

















The EBEX Balloon-borne Experiment—Gondola, Attitude Control, and Control Software

The EBEX Collaboration,

Asad Aboobaker¹, Peter Ade² , Derek Araujo³ , François Aubin⁴ , Carlo Baccigalupi^{5,6}, Chaoyun Bao⁴, Daniel Chapman³, Joy Didier³ , Matt Dobbs^{7,8}, Will Grainger⁹, Shaul Hanany⁴ , Kyle Helson¹⁰ , Seth Hillbrand³, Johannes Hubmayr¹¹, Andrew Jaffe¹² , Bradley Johnson³, Terry Jones⁴, Jeff Klein⁴, Andrei Korotkov¹⁰, Adrian Lee¹³, Lorne Levinson¹⁴ , Michele Limon³ , Kevin MacDermid⁷, Amber D. Miller³, Michael Milligan⁴, Lorenzo Moncelsi^{2,15} , Enzo Pascale², Kate Raach⁴, Britt Reichborn-Kjennerud³, Ilan Sagiv¹⁴ , Carole Tucker², Gregory S. Tucker¹⁰ , Benjamin Westbrook¹³, Karl Young⁴ , and Kyle Zilic⁴ 

¹ Jet Propulsion Laboratory, California Institute of Technology, Pasadena, CA 91109, USA

² School of Physics and Astronomy, Cardiff University, Cardiff, CF24 3AA, UK

³ Physics Department, Columbia University, New York, NY 10027, USA; didier.joy@gmail.com, derek@phys.columbia.edu

⁴ University of Minnesota School of Physics and Astronomy, Minneapolis, MN 55455, USA

⁵ Astrophysics Sector, SISSA, Trieste, I-34014, Italy

⁶ INFN, Sezione di Trieste, Via Valerio, 2, I-34127, Trieste, Italy

⁷ McGill University, Montreal, Quebec, H3A 2T8, Canada

⁸ Canadian Institute for Advanced Research, Toronto, ON M5G1Z8, Canada

⁹ Rutherford Appleton Lab, Harwell Oxford, OX11 0QX, UK

¹⁰ Brown University, Providence, RI 02912, USA

¹¹ National Institute of Standards and Technology, Boulder, CO 80305, USA

¹² Department of Physics, Imperial College, London, SW7 2AZ, UK

¹³ Department of Physics, University of California, Berkeley, Berkeley, CA 94720, USA

¹⁴ Weizmann Institute of Science, Rehovot 76100, Israel

¹⁵ California Institute of Technology, Pasadena, CA 91125, USA

Received 2016 September 12; revised 2017 February 22; accepted 2017 March 27; published 2018 November 6

Abstract

The E and B Experiment (EBEX) was a long-duration balloon-borne instrument designed to measure the polarization of the cosmic microwave background (CMB) radiation. EBEX was the first balloon-borne instrument to implement a kilopixel array of transition edge sensor (TES) bolometric detectors and the first CMB experiment to use the digital version of the frequency domain multiplexing system for readout of the TES array. The scan strategy relied on 40 s peak-to-peak constant-velocity azimuthal scans. We discuss the unique demands on the design and operation of the payload that resulted from these new technologies and the scan strategy. We describe the solutions implemented, including the development of a power system designed to provide a total of at least 2.3 kW, a cooling system to dissipate 590 W consumed by the detectors' readout system, software to manage and handle the data of the kilopixel array, and specialized attitude reconstruction software. We present flight performance data showing faultless management of the TES array, adequate powering and cooling of the readout electronics, and constraint of attitude reconstruction errors such that the spurious B -modes they induced were less than 10% of the CMB B -mode power spectrum with $r = 0.05$.

Key words: balloons – cosmic background radiation – cosmology: observations – instrumentation: polarimeters – polarization

1. Introduction

Measurements of the cosmic microwave background (CMB) have provided a wealth of information about the physical mechanisms responsible for the evolution of the universe. In recent years experimental CMB efforts have focused on polarization measurements. The polarization signals consist of two distinct patterns: E -modes and B -modes (Zaldarriaga & Seljak 1997). The level and specific shape of the angular power spectrum of CMB E -mode polarization can be predicted given the measured intensity anisotropy. Lensing of E -modes by the large-scale structure of the universe produces cosmological B -modes at small angular scales. An inflationary phase at sufficiently high energy scales near the big bang is predicted to leave another detectable B -mode signature at large and intermediate angular scales (Baumann et al. 2009).

The E -mode polarization of the CMB radiation was first detected by the Degree Angular Scale Interferometer experiment (Kovac et al. 2002). Other experiments soon followed suit (Scott

& Smoot 2010). The combination of all measurements is in excellent agreement with predictions. B -mode polarization from gravitational lensing of E -modes and from Galactic dust emission has also recently been detected (Hanson et al. 2013; Ade et al. 2014; Naess et al. 2014; BICEP2 Collaboration et al. 2014; BICEP2/Keck and Planck Collaborations et al. 2015). Intense efforts are ongoing by ground- and balloon-based instruments to improve the measurements, separate the Galactic from the cosmological signals, and identify the inflationary B -mode signature.

E and B Experiment (EBEX) was a balloon-borne CMB polarimeter striving to detect or constrain the levels of the inflationary gravitational wave and lensing B -mode power spectra. EBEX was also designed to be a technology pathfinder for future CMB space missions. To improve instrument sensitivity, we implemented a kilopixel array of transition edge sensor (TES) bolometers and planned for a long-duration

balloon flight. We included three spectral bands centered on 150, 250, and 410 GHz to give sensitivity to both the CMB and the galactic dust foreground. During first observations after reaching float, the instrument operated 504, 342, and 109 detectors at 150, 250, and 410 GHz, respectively. The combination of 400 deg² intended survey size and an optical system with 0^o.1 resolution gave sensitivity to the range $30 < \ell < 1500$ of the angular power spectrum. Polarimetry was achieved with a continuously rotating achromatic HWP.

Several new technologies have been implemented and tested for the first time in the EBEX instrument. It was the first balloon-borne experiment to implement a kilopixel array of TES bolometric detectors. It was the first to implement a digital frequency domain multiplexing system to read out the TES arrays; this digital system was later adopted by a number of ground-based experiments. The HWP was levitated using a superconducting magnetic bearing (SMB); this was the first operation of an SMB in an astrophysical instrument.

Design and construction of the experiment began in 2005. A 10 hr engineering flight was launched from Ft. Sumner, NM, in 2009, and the long-duration science flight was launched from McMurdo Station, Antarctica, on 2012 December 29. Because the majority of the 25-day long-duration flight was in 2013 January, we refer to this flight as EBEX2013.

This paper is one of a series of papers describing the experiment and its in-flight performance. The EBEX Collaboration et al. (2018a, hereafter EBEX Paper 1 (EP1)) discusses the telescope and the polarimetric receiver, The EBEX Collaboration et al. (2018b, hereafter EBEX Paper 2 (EP2)) describes the detectors and the readout system, and this paper, EBEX Paper 3 (EP3), describes the gondola, the attitude control system (ACS), and other support systems. Several other publications give additional details about the EBEX experiment. Some are from earlier stages of the program (Oxley et al. 2004; Grainger et al. 2008; Aubin et al. 2010; Milligan et al. 2010; Reichborn-Kjennerud et al. 2010; Klein et al. 2011; Sagiv et al. 2012; Westbrook et al. 2012), and others discuss some subsystems in more detail (Polsgrove 2009; Reichborn-Kjennerud 2010; Sagiv 2011; Aubin 2012; MacDermid 2014; MacDermid et al. 2014; Westbrook 2014; Zilic 2014; Chapman 2015; Chapman et al. 2015; Didier et al. 2015; Aubin et al. 2016; Didier 2016).

The requirements from a CMB polarimeter using a kilopixel array of TES bolometers with frequency domain multiplexing placed unique demands on the design and operation of the payload. In Section 2 we discuss the overall structure of the payload. We also describe the power system that was sized to provide a total power of at least 2.3 kW and a cooling system implemented to radiate the power dissipated inside four detector readout crates. Maintaining attitude control to the accuracy required by *B*-mode measurements is discussed in Section 3, and meeting the flight management challenges imposed by a kilopixel array operating aboard a balloon platform is discussed in Section 4.

2. Gondola: Mechanical, Power, and Thermal Management

2.1. Gondola Structure

We designed the EBEX gondola, shown in Figure 1, using heritage from past CMB balloon payloads, including the Millimeter Anisotropy eXperiment IMaging Array (Rabii et al. 2006) and the Balloon-borne Large-Aperture Submillimeter Telescope (BLAST; Pascale et al. 2008). The gondola

consisted of a rope-suspended outer frame that moved the entire gondola in azimuth and supported an inner frame containing the telescope and receiver that moved in elevation. The science payload weighed 2810 kg, not including NASA's Columbia Scientific Balloon Facility (CSBF) equipment and the flight train.

The main structures of both the outer and inner frames were made of 6061 aluminum for its high strength-to-weight ratio and ease of fabrication. The 449 kg outer frame structure consisted of these main elements: a pivot; three steel turnbuckles connecting the pivot to a triangular spreader; four ropes connecting the spreader to a rectangular (2.43 m × 1.68 m) table, made of structural I-beams; and A-shaped legs, formed from C-channels, sitting on the two far edges of the table and supporting the inner frame; see Figure 1. The table also held a reaction wheel, the flight computers, several coarse attitude sensors, attitude control electronics, and CSBF support electronics.

The 227 kg inner frame consisted of a structure made of box beams that was connected to the receiver and that supported the primary and secondary mirrors. The mirrors were attached to the inner frame by means of adjustable hexapods. The hexapods and the rest of the optical systems are described in EP1. Four bolometer electronic readout crates, two star cameras, and two three-axis gyro boxes were each mounted to the inner frame. The inner frame had a pair of 10.16 cm diameter aluminum pins with which the inner frame mounted to trunnion bearings on top of the A-shaped legs; see Figure 2. The pins were hard anodized for wear resistance. Each pin rotated in a 303 stainless steel pillow block mounted atop the trunnion legs. Lead bronze sleeves were pressed into each pillow block in order to reduce friction. The relative dimensions of the pin, the lead bronze sleeve, and the pillow block were such that over the expected temperature range the sleeve was always press fit in the pillow block while the pin had a diameter clearance that varied between 0.0122 cm at −60°C and 0.0066 cm at +40°C. To minimize stress on the pins due to misalignment, we ensured that the top surfaces of the trunnion legs were aligned such that the pins shared a common axis of rotation to within a tolerance of 0^o.1 (Reichborn-Kjennerud 2010).

To reduce payload weight, we used Plasma 12-strand ropes¹⁶ made with Spectra polyethylene fiber.¹⁷ To our knowledge, this was the first use of Spectra fiber ropes in a stratospheric balloon application. This raised two concerns. First, the strength of the ropes degrades with exposure to ultraviolet (UV) light. Second, the ropes undergo permanent lengthening, or creep, which increases with time, increased load, and temperature. To address these concerns, we conducted ground and flight tests to certify the ropes and quantify the creep and degradation from exposure to solar UV light. Laboratory measurements of rope creep over a 16-day period showed that the 508 cm ropes lengthened by 0.76 cm over a 9-day initial stretching phase, after which the rope length stabilized (Reichborn-Kjennerud 2010). Because the Antarctic flight ropes were prestretched while the gondola hung from the ropes during months of preflight testing, we assumed that negligible creep would occur during flight. To reduce the degradation in strength anticipated from solar radiation, we shielded the Antarctic flight ropes by wrapping them in two layers of aluminized mylar, each layer consisting of a 6.35 μm thick polyester film with a 50 nm thick

¹⁶ Puget Sound Rope Corp.

¹⁷ Honeywell International Inc.

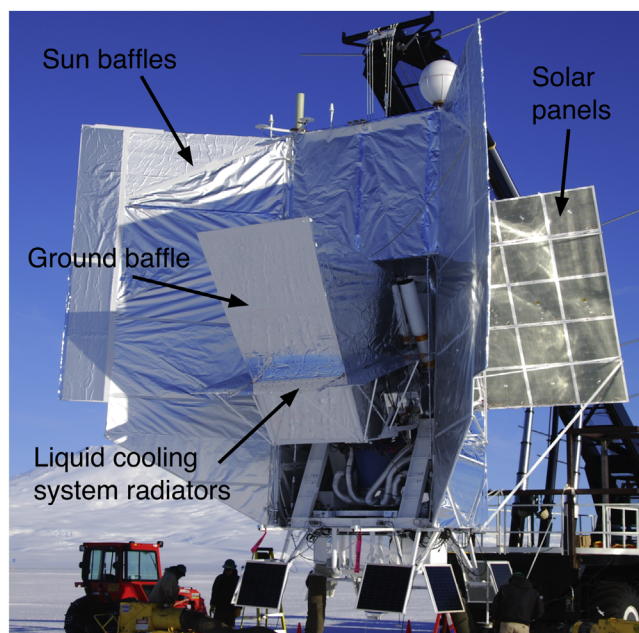
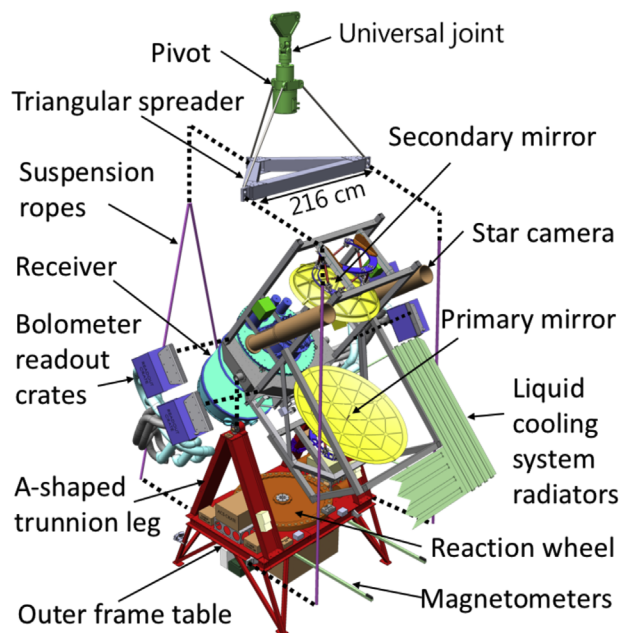


Figure 1. Left panel: exploded rendering of the EBEX gondola and main components of the instrument. Only the right side and half of the front liquid cooling radiators are shown. The other half has been removed for clarity. Right panel: photograph of the EBEX gondola before launch.

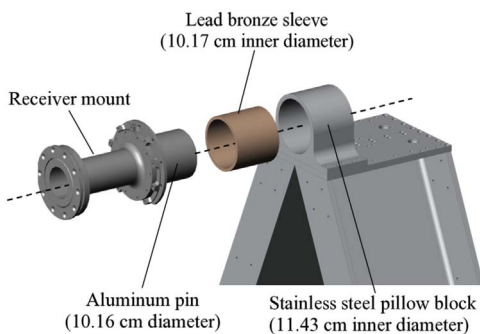


Figure 2. Exploded view of one of the two trunnion bearing mounts that supported the inner frame relative to the outer frame. The bronze sleeve was press fit into a stainless steel pillow block. The materials and diameters were chosen to ensure low friction under the broad range of temperatures encountered during payload ascent and flight.

layer of vapor-deposited aluminum. Tests of breaking strength conducted after a 28 hr rope certification flight launched in 2008 September from Ft. Sumner, NM, showed that the shielding provided significant protection against the degradation in the breaking strength; the bare ropes had an average degradation of nearly 10%, while the shielded ropes had a degradation of close to 2% (see Table 1). Assuming an exponential model, consistent with vendor ground testing data, we calculated the time constant for degradation at float and concluded that it would take 67 days for the breaking strength to decrease to the minimum level necessary to support a 10g vertical acceleration of the payload, as required by NASA.

We designed lightweight baffles to shield the telescope and receiver from direct illumination by the Sun and Earth. Baffles connected to the outer frame gave Sun protection when the azimuth of the telescope was within $\pm 60^\circ$ from anti-Sun and for all Sun elevation angles during any 24 hr period as long as the payload was at latitude southward of 73° south. Baffles

Table 1

Results from Breaking Strength Tests of Bare and Aluminum Mylar Shielded Spectra Fiber Ropes Flown during a 28 hr Certification Flight and Reference Rope (Not Flown)

Rope Tested	Breaking Strength (N)
Bare rope 1	220,000
Bare rope 2	228,000
Shielded rope 1	246,000
Shielded rope 2	240,000
Reference rope (not flown)	247,000

Note. The average degradation in breaking strength for the shielded ropes was 4000 N, while the average degradation for the bare ropes was 23,000 N.

connected to the inner frame provided protection from Earth for telescope elevation angles larger than 30° , which was the lowest nominal sky observation angle.

Each baffle surface contained two layers of aluminized mylar film¹⁸ in a strategy akin to that discussed by Soler et al. (2014). The outer layer used 50 nm thick vapor-deposited aluminum, and the inner layer used $8.9 \mu\text{m}$ thick aluminum foil bonded to a $50 \mu\text{m}$ thick mylar film. The mylar layers, which have high infrared emissivity and are thus responsible for radiating energy to space, were oriented such as to maximize the view factor to the open sky; see Figure 3.

We fabricated the 90 kg outer baffle structure from welded aluminum tubes designed for sufficient mechanical strength to support the triangle spreader and pivot when the suspension ropes were slack. To minimize weight, we fabricated the inner baffle from closed-cell extruded polystyrene foam and glued the aluminized films to the foam. Carbon fiber support structures would have been lighter but also significantly more expensive.

¹⁸ Lamart Corporation.

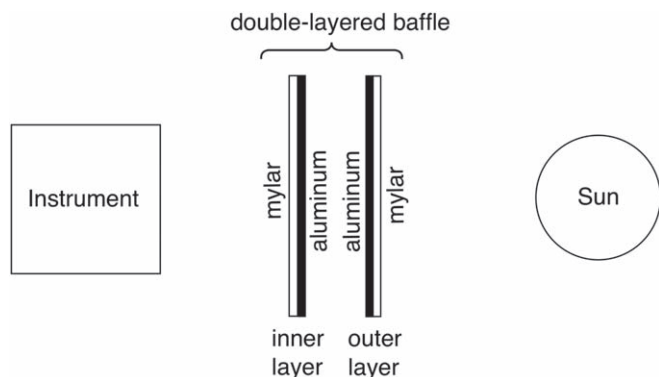


Figure 3. Surface orientation of the double-layered aluminized mylar baffles. Solar radiation is partially reflected and partially absorbed by the aluminum layer of the Sun-facing baffle. The mylar layer, which has high infrared emissivity, re-radiates the energy to space. A similar process occurs for the instrument-facing baffle for scattered solar radiation.

2.2. Gondola Motion Control

Azimuth motion control was achieved with an active pivot and a reaction wheel, each of which was driven by a brushless DC motor.¹⁹ In nominal motion, the pivot motor was intended to torque the entire gondola relative to the flight line and the balloon; the reaction wheel was to provide fine-tuning of azimuth motion. A detailed description of the azimuth control system can be found in Reichborn-Kjennerud (2010). The reaction wheel had a moment of inertia of 50.0 kg m^2 , approximately 1.6% of the total moment of inertia of the gondola. The pivot, shown in Figure 4, consisted of a shaft that was rigidly connected to a universal joint and from there to the flight train. The gondola was suspended on the shaft by means of two tapered roller bearings. The rotor of the motor was coupled to the shaft with bellows, obviating the need for precise axial alignment. All moving parts on the gondola were lubricated with low-temperature greases.²⁰

Because of an error in thermal design for the EBEX2013 Antarctic flight—see Section 2.4—the pivot motor controller overheated and shut down periodically, disabling control of azimuth motion. No such problems occurred during the North American 2009 engineering flight. A linear actuator²¹ provided elevation motion. The EBEX actuator had a 700 mm stroke and a maximum force of 3500 N and enabled a telescope elevation range of 17° – 68° (corresponding to an upright inner frame tower). We planned to observe the CMB above 30° elevation but maintained the capability for lower angles for observations of planets that are occasionally visible from Antarctica. The actuator was driven by a DC brush motor²² fitted with high-altitude brushes. To minimize the average force required from the actuator over the course of the flight, the inner frame was designed to be balanced with the cryogenics in the cryostat half full. Two motor drives of the same model²³ controlled the reaction wheel and the pivot motors, and an additional motor drive²⁴ controlled the linear actuator motor (Reichborn-Kjennerud 2010).

¹⁹ Kollmorgen Model D102M.

²⁰ Castrol Braycote 601EF, Dow-Corning Molykote 33 Light, or Mobil Mobilgrease 28.

²¹ SKF USA Inc. Model CARN32.

²² Pittman Motors Model 14207.

²³ ADVANCED Motion Controls Model DR-100RE.

²⁴ ADVANCED Motion Controls Model 30A8DD.

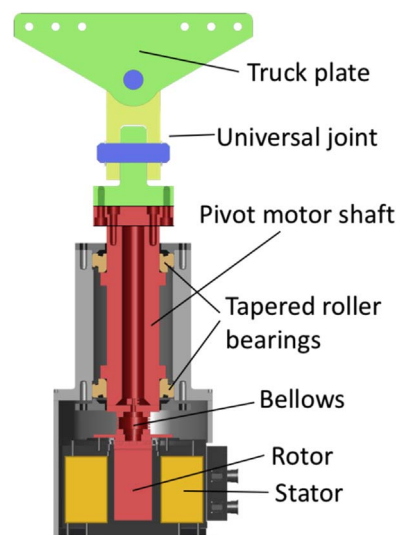


Figure 4. The pivot connected the flight train to the gondola and enabled active relative rotation. The flight train was connected to a truck plate, a universal joint, and a shaft. The gondola was suspended on the shaft by means of two tapered roller bearings. The rotor of a motor, whose stator was connected to the gondola, was coupled to the shaft with bellows.

To protect the elevation linear actuator from excessive loads during launch accelerations, we designed an elevation actuator protection mechanism; see Figure 5. The mechanism consisted of an inner frame locking pin driven by a 51 mm stroke actuator²⁵ and a spring-loaded latch pin attached to the bottom end of the actuator. During launch, we fixed the position of the inner frame with the locking pin and allowed the bottom end of the actuator to undergo limited motion. After launch, we fixed the bottom actuator end into operating position by engaging a spring-loaded pin and retracted the inner frame locking pin.

2.3. Power

Two separate systems generated and supplied power to the detectors and the rest of the electronics; the two systems shared only a single common electrical ground point; see Figure 6. The bolometer system provided power for detector biasing and readout, cryostat housekeeping and refrigerator control, and HWP readout and control. The ACS system powered the flight control computers, attitude control sensors and motors, data transmitters, liquid cooling system (LCS) pumps, and heaters for the sensors, motors, and batteries. Total peak power consumption was 1.7 kW as measured on the ground while connected to a power supply; see Table 2.

Each solar power system consisted of 15 solar panels²⁶ weighing 1 kg each and covering a total area of 8.6 m^2 . Each panel was specified to produce 76 W at float assuming orthogonal Sun, zero albedo, and an operating temperature of 110°C . Under these assumptions, the EBEX power system was capable of generating 2280 W. The power from each array of 15 panels was fed to a charge controller.²⁷ We replaced the controller heat-sink fin with an aluminum block heat sink directly to the gondola frame. We chose lithium-ion batteries for their high power density; the battery capacity for the

²⁵ Ultra Motion.

²⁶ Suncat Solar LLC.

²⁷ Morningstar Model TS-MPPT-60.

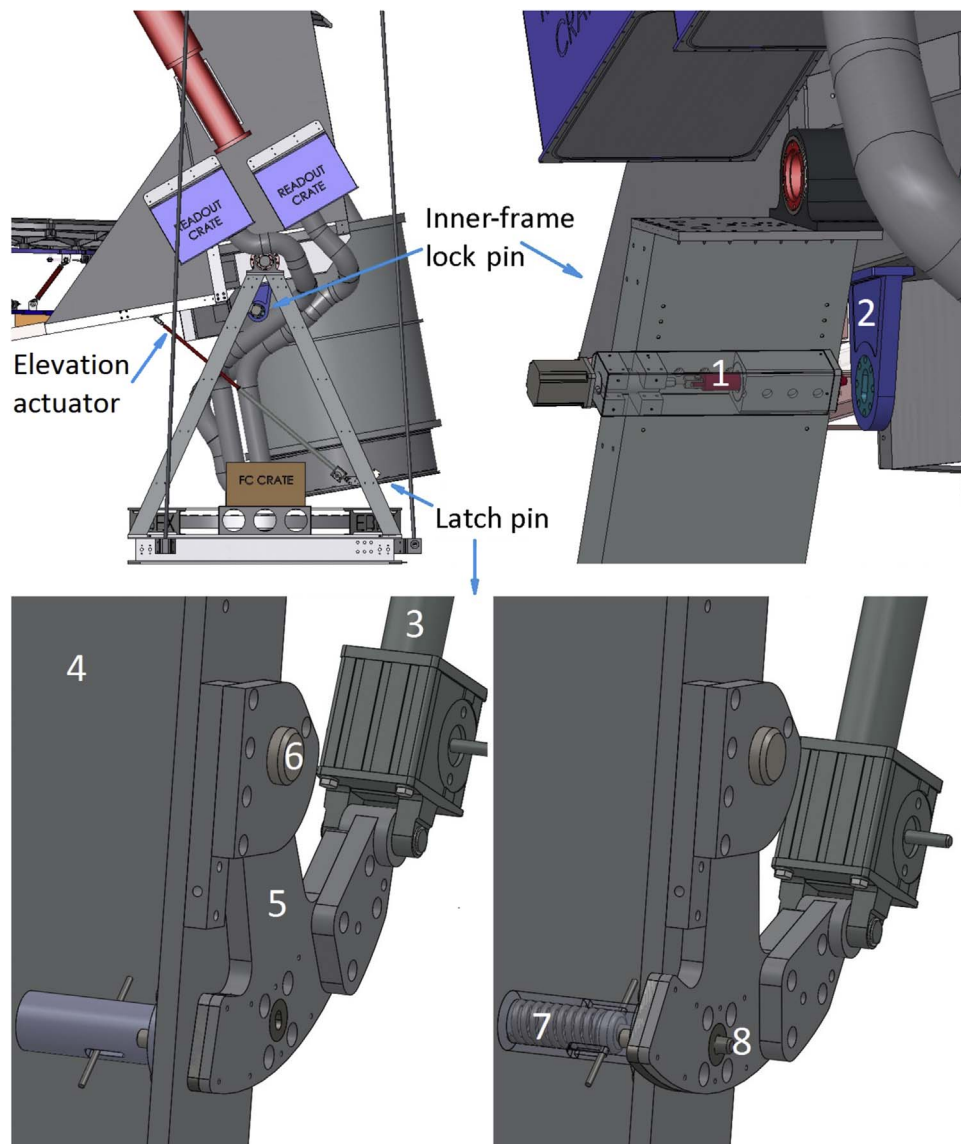


Figure 5. The elevation actuator protection mechanism (top left panel) had two elements, an “inner frame lock pin” (top right panel) and a “latch pin” (bottom). The inner frame lock (top right) locked the inner frame to the outer frame by means of a motorized, 2.54 cm diameter, steel pin (1). Before launch and before flight termination the motorized pin was commanded to engage into an inner frame bracket (2) that had a slot with tapered walls. But even as the inner frame was locked to the outer frame, it could experience elastic deformations exercising excessive axial loads on the elevation actuator. To protect the actuator, the latch was kept released (bottom left panel). The end of the actuator (3) was connected to the outer frame (4) via a bracket (5) that was allowed to rotate about a pin (6). After launch accelerations subsided, the elevation actuator was commanded to extend, bringing the hole in the bracket of the latch (5) into alignment with a spring (7) loaded pin (8), thus latching the actuator in place (bottom right panel). The motorized pin of the inner frame lock (1) was then retracted, releasing the inner frame.

detector and ACS power domains was 208 and 144 Ahr, respectively, and the nominal voltage of each system was 28 V.

The batteries included built-in control electronics that provide temperature, voltage, and current monitoring. They also included a mechanism to open the battery’s main switch in case of a detected fault. We disabled this feature because we found that it generated fault detections even under normal conditions.

To specify the proper solar panel area and battery capacity, we produced a simulation of the power system throughout the flight, from the prelaunch hands-off period on the ground through ascent and successive CMB and calibrator scans at float. Because the instrument did not complete the scan strategy as planned during flight (see Section 2.4), we evaluate the power system performance by comparing the minimum battery capacity predicted by the simulation to that reached after

ascent, during which the gondola spun in full rotations, as expected and simulated.

To ensure that we did not underestimate the required battery capacity, we conservatively assumed a 35% albedo and 110°C panel temperature in our simulation. (Solar power production was expected to degrade by 0.4% for every 1°C increase in temperature.) Under these assumptions, the simulation predicted a minimum battery state of charge of 40% when the payload reached float altitude. Problems with the battery electronics readout prevented reliable monitoring of all but one of the five batteries. That battery’s measured state of charge decreased from 94% to 91% during ascent. The difference from the simulation is explained by the fact that the actual albedo was probably closer to 100%. Also, the actual solar panel temperature ranged between -15°C and $+60^{\circ}\text{C}$. During flight, the battery reached a minimum state of charge of 65% during

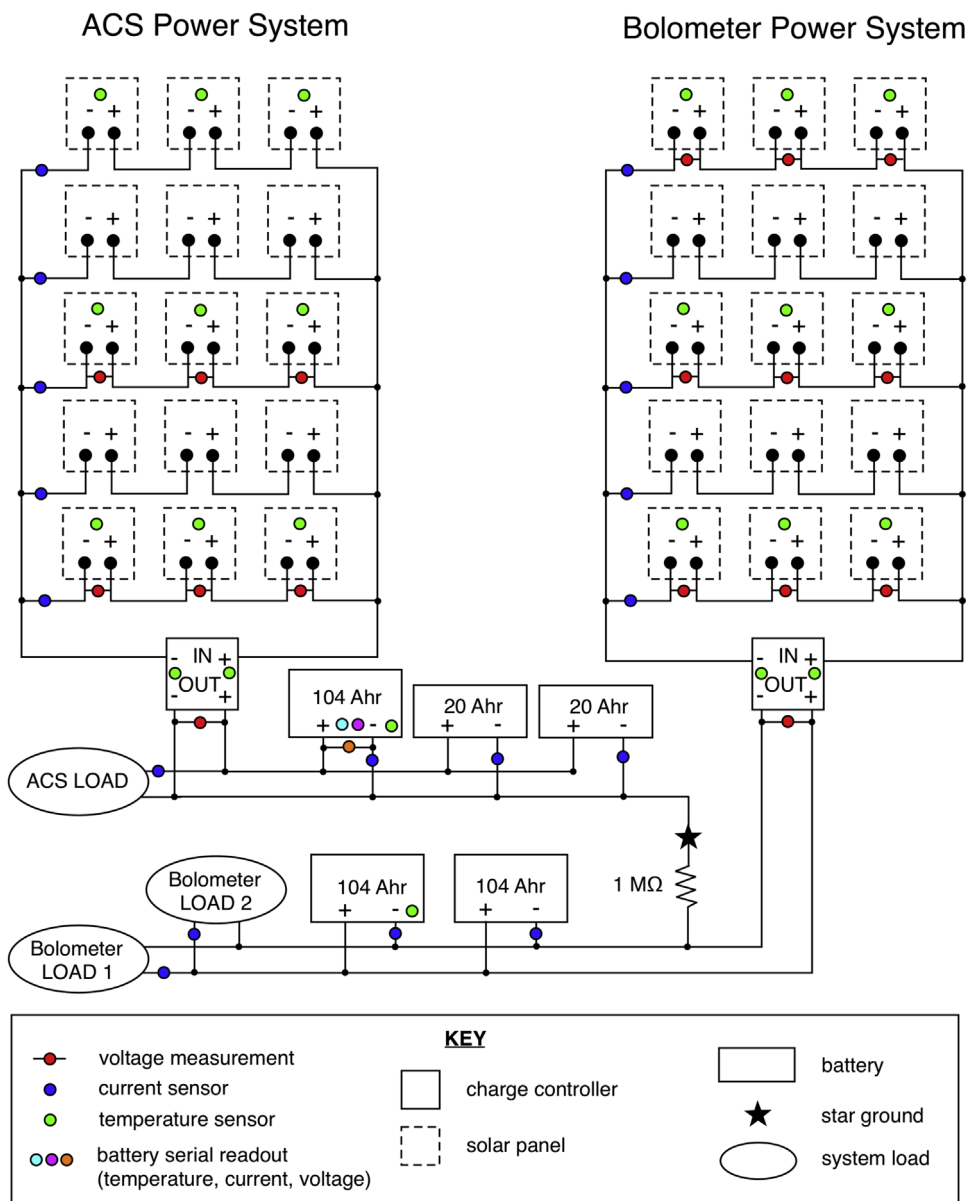


Figure 6. Schematic of the ACS and bolometer power systems. The two power systems shared a common electrical ground, marked here with a star (★). Each 28 V power system contained high-capacity lithium-ion batteries (with respective charge capacities of 144 and 208 Ahr), charged by 15 lightweight solar panels (each weighing 1 kg and specified to produce 76 W).

the first day of flight and generally remained between 85% and 100% charged.

2.4. Thermal Management

2.4.1. Instrument-wide Overview

An engineer working with NASA’s CSBF performed a thermal analysis of the entire instrument, taking into account the radiation from the Sun and Earth at float, the minimum and maximum power dissipated in each component, electrical enclosure surface coverings, radiation scattering due to the atmosphere, and the thermal conductivity of the air at float altitude. For this analysis the engineer used values for Earth’s albedo and long-wavelength radiation that are up to 2.3σ higher and lower than measured means, such that the extreme values would occur in only 2% of the cases. This analysis yielded the extreme temperatures that are

likely to be encountered by any piece of hardware aboard the payload. When the simulation indicated that components would exceed their specified operating ranges, we added heaters or improved cooling, as necessary. We then used thermal vacuum tests to ensure that each component would operate within its required temperature range. In order to minimize infrared absorption by bare aluminum surfaces, the entire gondola frame was white powder coated; some electronics enclosures were painted with white Krylon Appliance Epoxy,²⁸ while for others we used silver Teflon tape.²⁹

During flight, the pivot motor controller overheated and automatically shut itself down when we attempted to execute the planned scan strategy. The overheating resulted from a thermal model error that led to inadequate cooling of the pivot

²⁸ Sherwin Williams Company.

²⁹ Sheldahl fluoro-ethylene propylene tape by Multek Corporation.

Table 2

Power Consumption by the EBEX Instrument ACS and Bolometer Power Systems as Measured on the Ground While Connected to a Power Supply

Component	Power Consumption (W)
ACS Power System	
Flight computer and data storage	189
Sensors	135
Motors	66
Liquid cooling system pumps	40
Line of sight video and data transmitters*	181*
Heaters (sensor, motor, and battery)*	325*
Total peak power consumption	936
Bolometer Power System	
DC–DC bias crate	137
Bolometer readout crates (4 units)	586
Cryostat housekeeping and refrigerator control	46 (7*)
Half-wave plate crate	32
Total peak power consumption	801

Note. Components marked with an asterisk (*) consumed power only intermittently. Data and video transmitters were active only during the first 24 hr. Heaters were active primarily during payload ascent. Out of the 46 W consumed for cryostat housekeeping and refrigerator control, 7 W were expended only during refrigerator cycling. Without these intermittent components total power consumption was 1224 W.

motor controller, which was exposed to direct sunlight. The error, which went undetected throughout payload development, was introduced when the gondola solid model was imported into the thermal model. As a result, the azimuth control system did not perform as designed, so (i) we were unable to observe the originally planned sky region and (ii) some instrument components operated in an unanticipated radiative environment for a prolonged period. Nevertheless, when the telescope was pointed away from the Sun, all instrument components except the pivot motor controller operated within the expected temperature range, validating all other elements of the thermal design.

2.4.2. Liquid Cooling System

For detector readout we used 28 digital frequency domain multiplexer (DfMUX) boards distributed among four bolometer readout crates (BRCs). Two BRCs had six and two had eight boards each. The four BRCs with all the DfMUX boards operating, superconducting quantum interference devices (SQUIDs) tuned, and all bolometers overbiased drew 723 W from the power system, of which 593 W were dissipated inside the BRCs and the rest were dissipated in a separate power crate that housed the 82% efficiency DC–DC converters. The 21 W per board were dissipated mostly by a field-programmable gate array (FPGA) on the motherboard and by digital-to-analog converters (DACs) and analog-to-digital converters (ADCs) on each of two mezzanine boards that were plugged into the motherboard. Each of these two sources—FPGA and DAC/ADC—was encased with an RF enclosure. We designed a thermal cooling system to move the dissipated energy from the hot components to their RF enclosure and then from the RF enclosure to the back of the BRC and to the ambient environment. Figure 7 gives the details of the approach we used.

To provide thermal connection between the FPGA and the RF cage, we used a thermally conductive compound.³⁰ For the DAC/ADC and amplifiers on the mezzanine boards we used small copper bars and thermal interface pads³¹ with a thin layer of the thermal compound. We used flat heat pipes³² that were glued with thermal adhesive compound³³ to the RF cages to transfer the energy to a copper tab at the edge of the board. The copper tab was pressed into a slot on the top of the BRC that also hosted a liquid cooling loop.³⁴ The liquid transferred the heat to radiator panels that had a total area of 4.1 m².

During preflight vacuum chamber tests, we measured a 45°C temperature difference between the DfMUX motherboard and the BRC wall. The LCS and the area of the radiators were designed to maintain the top of the BRC wall below 25°C so as to maintain the DfMUX electronics below the most stringent component specification limit of 70°C. The LCS consisted of two independent closed loops, each responsible for dissipating heat from two BRCs. In each loop we employed a 20 W, 80 psi differential pressure pump³⁵ to circulate the coolant³⁶ and a reservoir to accommodate pressure variations and prevent bubbles. We bolted multichannel extruded aluminum heat exchangers to the radiator panels and applied a thin layer of thermally conductive silicone grease³⁷ between the extrusions and the panels. The total length of tubing for each LCS loop was 13.3 m, and the average diameter was 4.75 mm. At an average coolant flow of 30 mL s⁻¹ the heat transfer between the bulk of the liquid and the heat exchangers, as well as the dynamics of the coolant in the tubes, were consistent with the regime of weak turbulence. The pressure gradients across the LCS elements were in a good agreement with the turbulent model predictions, with a friction factor corresponding to an average wall roughness of 0.1 mm. The radiators dissipated the heat to space with an average view factor of 0.52. To minimize solar absorptance and enhance infrared emittance, we covered the panel surfaces with silver Teflon tape³⁸ with solar absorptance $\alpha \leq 0.10$ and infrared normal emittance $\epsilon \geq 0.80$.

During flight, the LCS kept the readout boards within the required temperature range despite periodic exposure of the radiator panels to direct sunlight due to the gondola rotational motion (as described in Section 3). Figure 8 shows the temperature of the BRC top plate along with the temperature of the enclosed DfMUX boards during a representative segment of the flight. The nearly 10°C observed difference between the warmest and coolest DfMUX boards is due to the difference in radiative environment for the inner and outer boards inside the crate. The boards in an eight-board (six-board) BRC were warmer by approximately 40°C (30°C) relative to the exterior of the crate (MacDermid 2014).

3. Attitude Determination and Control

The ACS consisted of sensors, actuators, and a set of control algorithms operating in a feedback loop. Its role was to determine the instantaneous attitude of the telescope and

³⁰ Arctic Silver 5 by Arctic Silver.

³¹ Part 5519S by 3M.

³² NanoSpreaders made by Celsia Technologies.

³³ Arctic Silver Thermal Adhesive by Arctic Silver.

³⁴ Lytron CP15 by Lytron.

³⁵ Micropump GJ Series.

³⁶ Dynalene HC-40 by Dynalene, Inc.

³⁷ Chemplex 1381.

³⁸ Sheldahl fluoro-ethylene propylene tape by Multek Corporation.

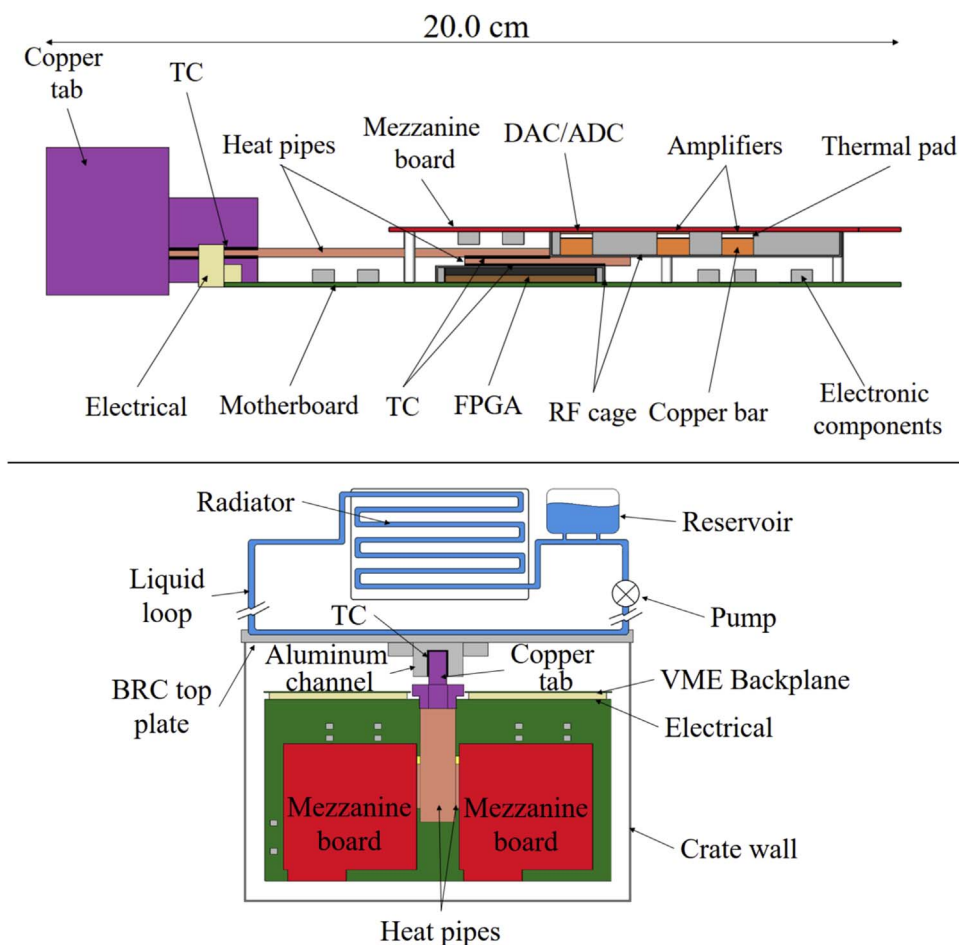


Figure 7. Top panel: side view and scale bar of a readout board and its heat-dissipating and conducting components. Lower panel: sketch of the entire thermal pass, including a top view of a readout board, the liquid cooling loop, and radiator panels. Power dissipated by the FPGA on the motherboard (top panel, brown) was transferred to its RF cage via thermal compound (TC). Power dissipated by the DAC/ADC on the mezzanine boards was transferred to the RF cage via intermediate copper bars (orange) and thermal interface pads (white) with a thin layer of thermal compound. Two flat heat pipes (salmon) that were glued to the RF cages conducted power to a copper tab (purple) that pressed into a channel in the BRC top plate (bottom panel, gray). A liquid coolant transferred the power to external radiator panels.

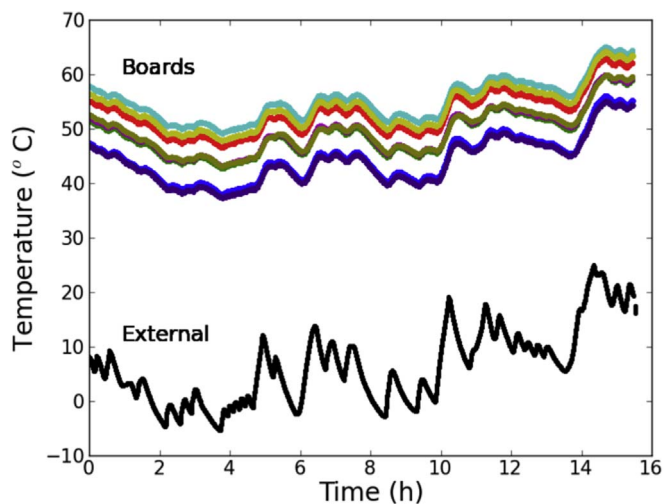


Figure 8. Temperature of a BRC top plate (“External”) and of the eight enclosed DfMUX boards over a 16 hr period. Fluctuations of the External sensor strongly correlate with Sun orientation. The boards’ temperature fluctuations are a low-pass-filtered version of the External sensor’s owing to the thermal conductance and heat capacitance of the liquid coolant. The warmer boards were located toward the middle of the crate, while the cooler boards were located closer to the ends of the crate. Only five of the board temperature traces are clearly visible in this plot, as three traces overlap closely with others.

execute a predefined sky scan pattern. It also acquired and stored the data required for post-flight attitude reconstruction. A block diagram of the ACS is shown in Figure 9. We present the main elements of the system, focusing on the sensors and the control algorithms. We summarize the performance of the ACS during the 2013 flight and the post-flight attitude reconstruction. The actuators are described in Section 2.2. Elements of the EBEX ACS are also described in several additional publications (Chapman 2015; Chapman et al. 2015; Didier et al. 2015; Didier 2016).

3.1. Attitude Sensors

The ACS sensors consisted of two redundant star cameras, two redundant three-axis rate gyroscopes, two Sun sensors, two redundant magnetometers, a differential global positioning system (dGPS), an elevation encoder, and an inclinometer. We also had access to information provided by the dGPS of the CSBF. Table 3 summarizes the specifications and model of each sensor.

The primary sensors used for both real-time control and post-flight attitude reconstruction were the star cameras and gyroscopes. The star cameras were mounted on either side of the inner frame and were approximately aligned with the telescope beam. The two gyroscope boxes, each consisting of

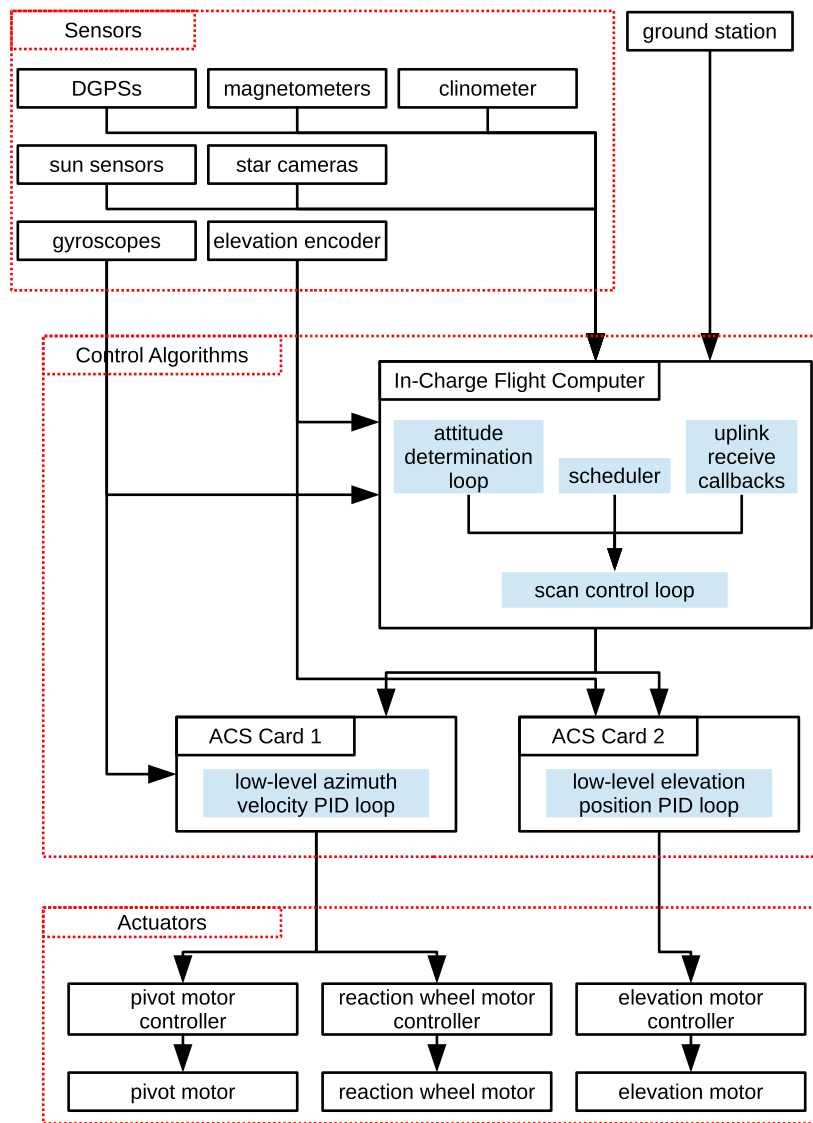


Figure 9. The EBEX ACS consisted of three main components (red boxes): attitude sensors, control algorithms, and actuators. The sensors measured the instantaneous attitude, either absolute or relative to the gondola. The control algorithms processed this information to estimate the telescope attitude, compare it to a desired attitude as determined by a user-defined scan strategy, and issue instructions to actuators. Filled blue boxes represent software/firmware loops. Black bordered boxes represent physical components. Arrows represent the flow of data.

Table 3
List and Specification of Attitude Sensors

Sensor	Model Name	Quantity Flown	Direction of Attitude Provided	In-flight Precision	Sample Rate
Star camera	Kodak KAF-1603E Canon EF 200 mm f/1.8	2	az, el and roll	1''3 57''	Up to 0.5 Hz
Magnetometers	Meda TFS 100	2	az	1°	5 Hz
Sun sensors	Hamamatsu S5991-01	2	az	0°8	5 Hz
Differential GPS	Thales ADU 5	1	az	0°5	5 Hz
Inclinometer	Geomechanics 904-T	1	el	0°5	100 Hz
Encoder	Gurley A25S	1	el	0°2	100 Hz
Gyroscopes	KVH DSP 3000	6	3-axis rates	40'' s ⁻¹	1000 Hz

Note. The “precision” gives the standard deviations of the distributions in Figure 11 for the star camera, and Figure 12 for other sensors.

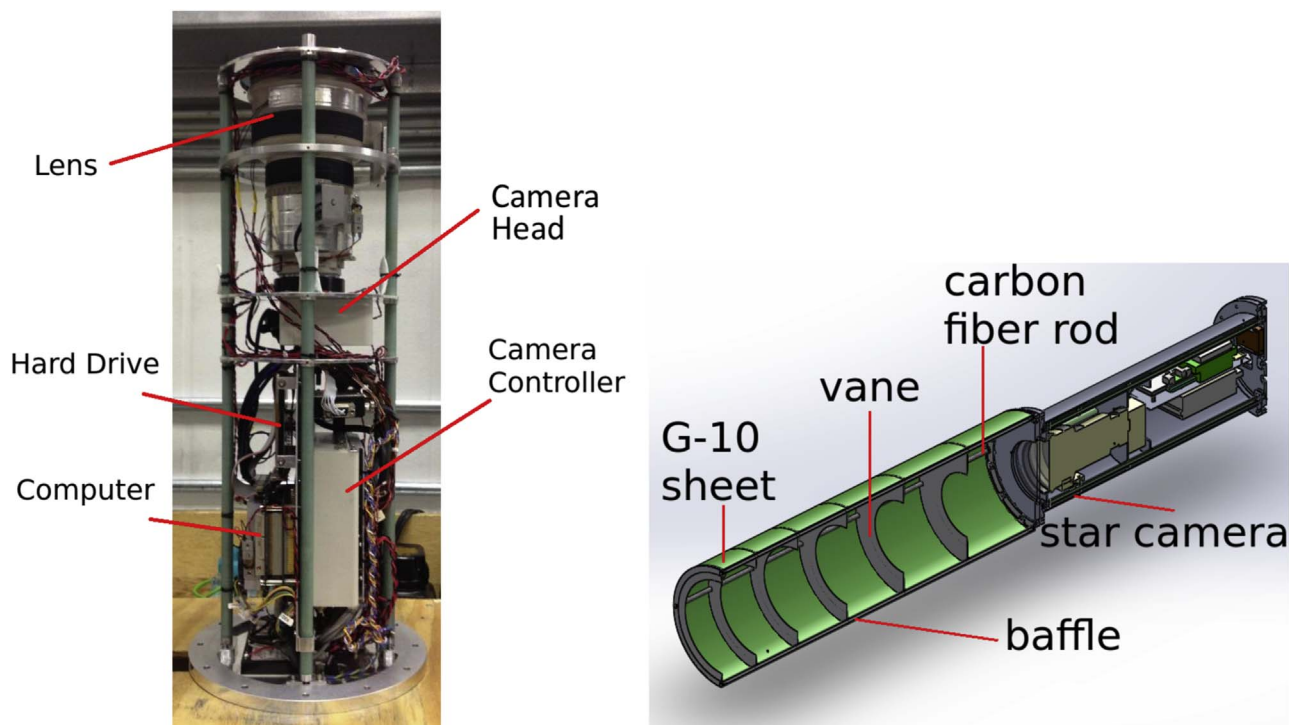


Figure 10. The star camera assembly consisted of a pressurized vessel that held the star camera hardware and a baffle (right). The baffle was made of an 87.6 cm long tube of G-10 fiberglass sheet that was wrapped around thin aluminum vanes connected with carbon fiber tubes. The baffle weighed 1.87 kg. Inside the vessel (left), which was pressurized with N_2 gas to 1 atm, were the camera head, lens, camera controller, and computer.

three nearly orthogonal fiber-optic gyroscopes, were also mounted on the inner frame.

Each star camera consisted of a telephoto lens, a filter,³⁹ a charge-coupled device camera, and a computer mounted in a rigid assembly inside a cylindrical vessel filled with nitrogen gas at a pressure of 1 atm. A stray-light baffle was mounted to the exterior of the star camera pressure vessel; see Figure 10. All parts inside the baffle were painted with flat black spray paint.⁴⁰ The star camera found an attitude by taking a picture of a star field and comparing the image to a star catalog. The two star cameras were redundant to ensure that attitude solutions were available even if one failed. The star camera computer ran the Star Tracking Attitude Reconstruction Software (STARS), a platform-independent software custom-written for EBEX in C++ that captured the images, found the bright spots in the image, matched their pattern to a known catalog of stars, and communicated the resulting solution to the flight control program (FCP) operated by the main flight computer (Chapman et al. 2014). STARS was optimized to find stars even when the camera was out of focus or when the stars were blurred owing to gondola motion. Each camera had a point-spread function with an FWHM of $9''$ and a field of view of $4^\circ 05' \times 2^\circ 70'$. Star camera exposure time was set to 300 ms in order to reliably detect stars with apparent magnitude 7.3 or brighter. With this exposure time, the motion blur solving feature of STARS permitted the cameras to solve images taken with azimuthal velocities up to $0^\circ 02 \text{ s}^{-1}$.

The star cameras performed well during flight, consistently solving the images in real time with minimal intervention. The STARS software overcame several unanticipated challenges:

- (a) The loss of azimuth control (see Section 3.3) prevented STARS from performing the autofocus algorithm, which required stationary pointing, and both star cameras were slightly out of focus during the entire flight. STARS continued to find stars in the images, however, because of its robust source detection algorithm.
- (b) To solve images quickly, STARS normally used a coarse attitude determination by the secondary sensors. The coarse approximation minimized the search radius when matching the stars in the image to the catalog of stars. The dGPS failed to provide information for multiple sections of the flight, which prevented the attitude guess from the secondary sensors from being transformed from the local az/el reference frame to the equatorial reference frame in which the cameras operated. Yet even in those sections STARS continued finding solutions within several seconds, switching to its “lost-in-space” mode. The STARS catalog was optimized by precomputing the distances between combinations of stars and by filtering the catalog down to fewer than 20 stars per field of view. Without the optimizations implemented in STARS, finding solutions without directional guidance could take a few minutes per image (Chapman 2015).
- (c) The STARS software successfully identified stars and matched stellar patterns in the presence of image nonidealities, including passing polar mesospheric clouds, vignetting, and internal reflections (Chapman 2015).

The two star cameras acquired a total of 41,262 images, 80% of which provided attitude solutions post-flight. Most of the remaining images were saturated because the cameras were pointing at the balloon during housekeeping operations or the attitude was within 30° of the Sun. On average there were eight

³⁹ Red color 25A filter from Hoya Filters.

⁴⁰ Krylon Ultra-Flat Black.

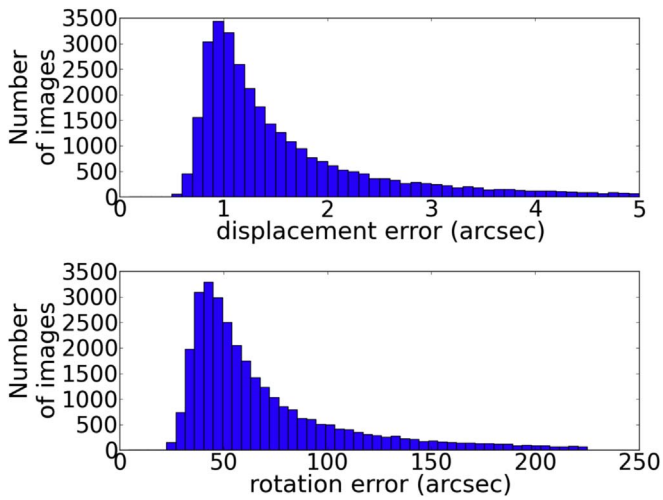


Figure 11. Histogram of the attitude solution uncertainty as reported by the pattern matching least-squares algorithm for all solved images. The top panel shows the displacement uncertainty, i.e., the combined uncertainty from $RA \times \cos(\text{decl.})$ and decl. The bottom panel shows the rotation uncertainty around the image center. The median uncertainty is $1''.3$ in displacement and $57''$ in rotation.

stars per image. Figure 11 shows a histogram of the solution uncertainty from all solved flight images. The uncertainty was reported by the least-squares algorithm matching the pattern of stars in the image to the catalog.

Each gyroscope measured the rate of angular rotation around its axis and outputted a digital signal at 1000 Hz that was read out by an onboard digital signal processing (DSP) unit.⁴¹ The data were despiked, passed through a box-car infinite impulse response filter with a cutoff frequency of 20 Hz, and written to disk at 100 Hz. The gyroscopes were chosen for their combination of cost, their relatively low white noise ($40'' \text{ s}^{-1}$), and their bias timescale of ~ 200 s. Three gyroscopes were mounted inside a precision machined aluminum box with connecting surfaces orthogonal to within $5'$. The gyroscopes were wrapped in overlapping strips of magnetic shielding⁴² to reduce their susceptibility to ambient magnetic fields. The shielding reduced the gyroscopes' zero-motion bias from $17'' \text{ s}^{-1} \text{ G}^{-1}$ to $3'' \text{ s}^{-1} \text{ G}^{-1}$ (Reichborn-Kjennerud 2010). The gyroscopes performed well during flight, recording data continuously and exhibiting white noise and bias behavior in accordance with preflight measurements.

As listed in Table 3, EBEX also flew a complement of secondary sensors designed to provide coarse real-time attitude to be used as a pointing guess for the star cameras and intended to provide backup in case the star cameras failed to solve images in real time. The main source of error for real-time attitude determination using the coarse sensors was the calibration of each sensor's overall directional offset. Before flight, we measured these offsets by referencing the sensors to star camera solutions obtained using the few stars bright enough to be visible by the star camera from the ground during the Antarctic summer. Directional offsets were recalibrated periodically in flight using the star camera solutions. Figure 12 gives the in-flight performance for each of the secondary sensors given the calibration performed *preflight* and ignoring all in-flight recalibrations. This is a “worst-case scenario” indicating what the performance of the sensors

would have been had the star cameras not provided any recalibration during flight. The dispersion about the mean of each sensor is an indicator of each sensor precision over more than 10 days of flight, and the mean of each sensor is an indicator of the accuracy of the *preflight* calibration.

3.2. Control Algorithms

Three subprograms operated in a feedback loop to control the instrument attitude (see Figure 9): the attitude determination subprogram used sensor information to estimate the telescope attitude, the scan pattern subprogram determined the instantaneous desired attitude and scan rate, and the low-level subprogram sent current to the azimuth and elevation actuators. The attitude determination and scan pattern subprograms ran on the “in-charge” flight computer—one of the two redundant flight computers (see Section 4.1)—at 100.16 Hz. The azimuth and elevation low-level subprograms ran on two DSP cards⁴³ at 10,400 Hz.

The attitude determination subprogram estimated the telescope attitude by performing a weighted average of the information obtained from all sensors deemed operational by ground operators. Horizontal roll was approximated as zero. Each sensor's attitude information was estimated using a 1D Kalman filter that evolved the sensor prior attitude using the gyroscopes' data and included new available measurements.

The primary scan pattern was a raster scan. The algorithm to perform this scan was a state machine that alternated between scanning at constant azimuth velocity, pausing to capture star camera images, and stepping to the next elevation. Given the scan parameters and the current attitude, the algorithm output was a target azimuth velocity and target elevation position at every time step.

The requested velocities and attitudes were transmitted to the DSPs, which had proportional-integral (PI) feedback loops operating on the difference between current and target quantities (Didier 2016). The outputs of the PI loops were ultimately converted to a pulse-width-modulated (PWM) signal for the motor controllers. The PI values were tuned in flight to ensure optimal motion of the telescope. The feedback loops had override modes that allowed the ground operators to command PWMs manually. In flight, we employed both manual PWMs and the automatic scan algorithms.

3.3. In-flight Performance

The EBEX payload launched from McMurdo, Antarctica, on 2012 December 29. It circumnavigated the continent, taking data for 11 days at an average altitude of 35 km. Shortly after reaching float altitude, we discovered that the pivot motor controller was overheating and shutting down (see Section 2.4.1). Without active control, the azimuth of the gondola was determined by the rotation of the balloon and the rotational spring constant of the flight train. The resulting azimuth motion is shown in Figure 13. It was a superposition of full rotations with variable rotational speed and 80 s period oscillations that had variable amplitude. Throughout the flight, more than 97% of the azimuthal speeds were below 1° s^{-1} . We oriented the gondola at constant elevation of 54° in order to maintain an angular separation of $\sim 15^\circ$ between the telescope boresight and both the balloon and the Sun's maximum elevation. The resulting sky coverage was a strip

⁴¹ Provided by the University of Toronto.

⁴² Metglas, Inc.

⁴³ ADSP 21062 from SHARC by Analog Devices, Inc.

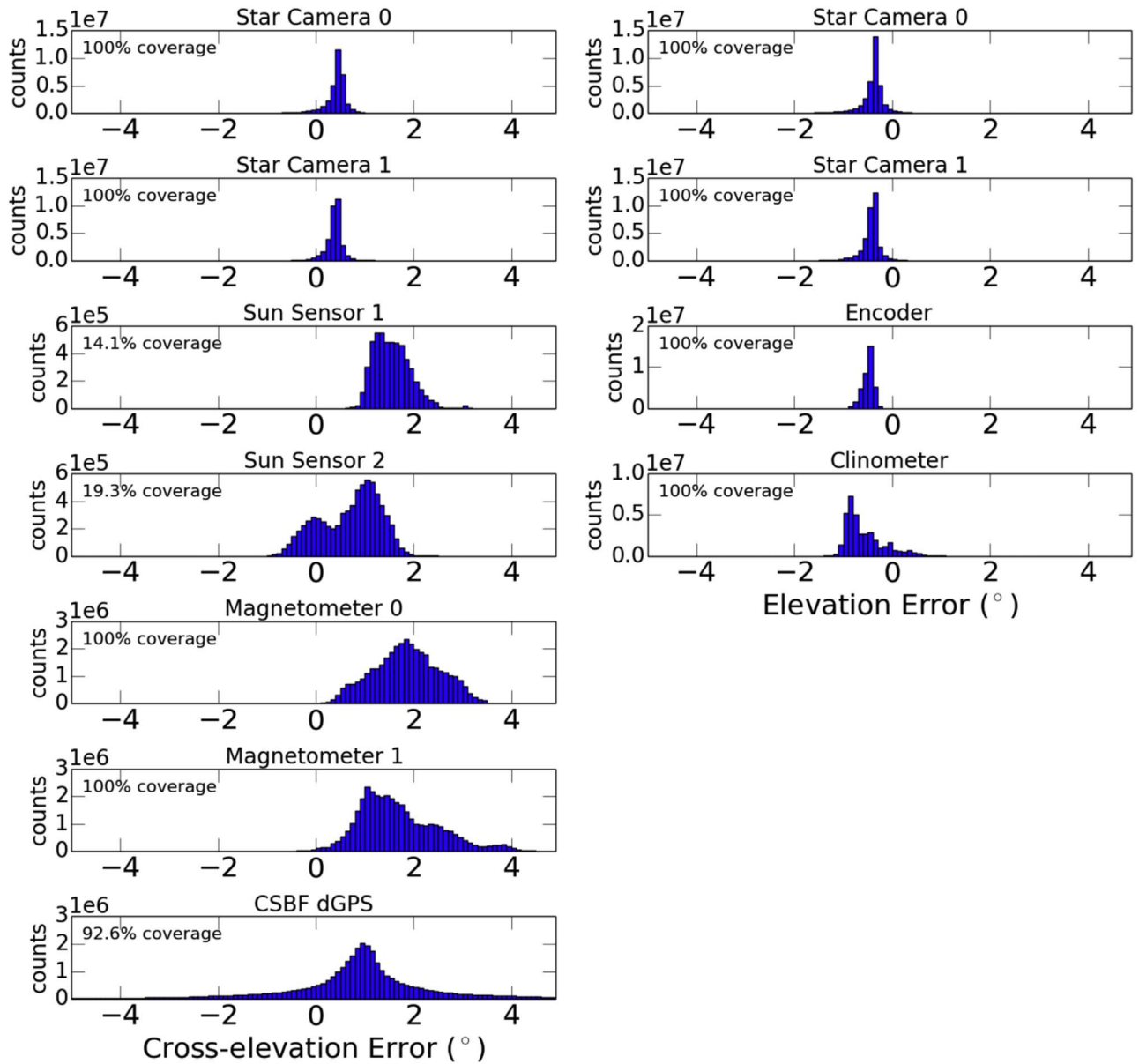


Figure 12. Performance in cross-elevation (defined as $\text{azimuth} \times \cos(\text{elevation})$; left column) and elevation (right column) of each absolute pointing sensor during the EBEX2013 flight given the *preflight* calibration procedure. Cross-elevation is calculated using the post-flight elevation. Each plot shows a histogram of the difference between the post-flight reconstructed boresight attitude and the in-flight sensor attitude computed using preflight offset calibration. Coverage values give the percentage of time the sensor provided valid attitude. The EBEX dGPS is not plotted, as it failed early in flight and did not provide attitude.

of sky delimited by decl. $-67^\circ 9'$ and $-38^\circ 9'$, covering an area of 5700 deg^2 ; see Figure 13. By a fortunate coincidence, the 80 s natural rotational oscillation period of the gondola and flight line matched the designed scan strategy. Thus, the gondola came to a stop every ~ 40 s, enabling star camera images to be taken while the gondola was in the stationary position that is optimal for star camera imaging. In this manner, all the preflight work of assessing attitude determination accuracy was still relevant to the actual scan pattern of the EBEX2013 flight.

3.4. Post-flight Attitude Determination

Errors in attitude determination convert E -mode to B -mode signal. To keep these spurious B -modes negligible, we placed a requirement that the spurious B -modes would be less than 10% of an inflationary B -mode with $r = 0.05$ and nominal

cosmology lensing signal within $30 \lesssim \ell \lesssim 1500$, which was the range the instrument was designed to probe. Hu et al. (2003) quantified the effects of several types of experimental errors, including attitude errors, on the determination of the B -mode power spectrum. In their formalism, attitude errors are characterized in terms of their spatial power spectral density, and the induced B -modes are given in terms of a convolution with the cosmological E -modes. In this section we discuss the approach we used to reconstruct attitude post-flight and quantify the attitude errors. We refer to the entire pipeline as attitude determination software (ADS). Didier (2016) used the ADS to construct the spatial spectral density of the measured attitude errors, convolved it with the cosmological E -modes, and showed that the requirement on attitude reconstruction for the EBEX2013 flight has been met.

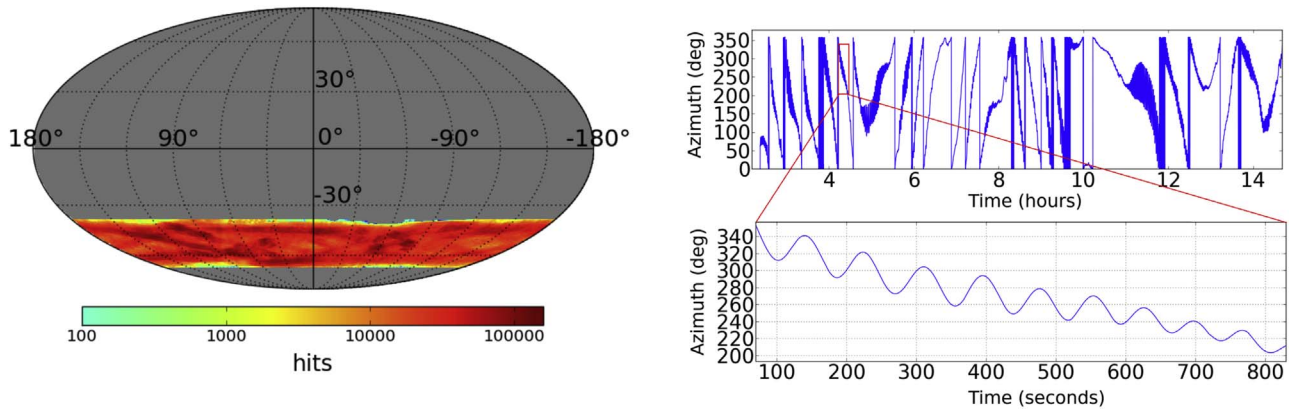


Figure 13. Left: map in equatorial coordinates of the number of detector samples per pixel (hit map) for the EBEX2013 flight from all frequency bands. Right: typical patterns in the azimuth motion during the EBEX2013 flight. Over long timescales the gondola executed full 360° rotations with occasional reversal of direction (top panel). Superposed was an oscillatory motion (bottom panel) with 80 s period. This period matched the one predicted given the moment of inertia of the gondola and the torsional constant of the flight line. This rotational motion had variable amplitude that reached up to tens of degrees.

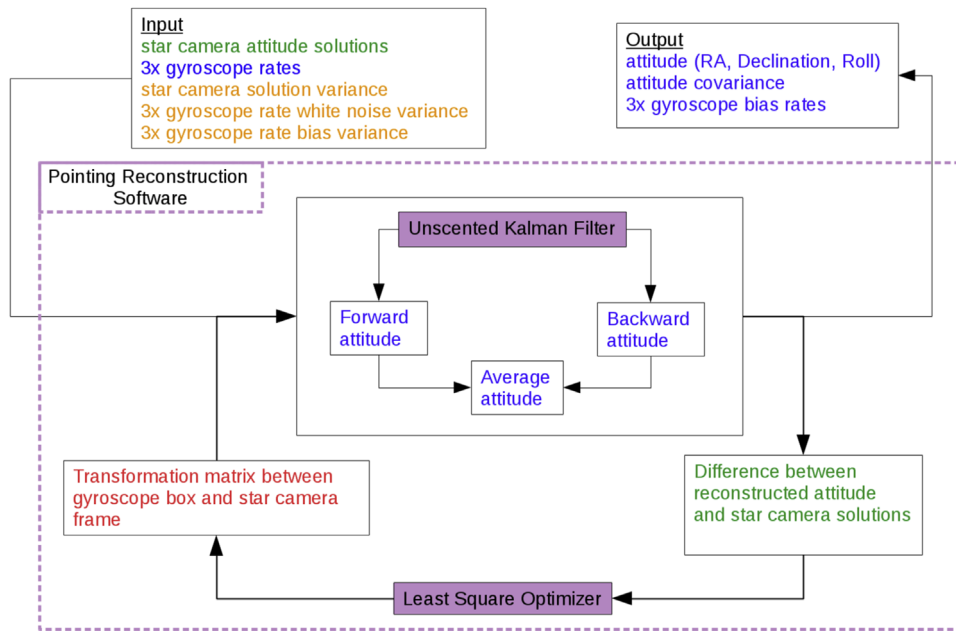


Figure 14. Diagram of the ADS. The filled purple boxes denote the two primary constituent codes. The blue text designates arrays of data with identical lengths and a sample rate of 100.16 Hz. The green text represents much smaller arrays with length equal to the number of star camera solutions. The yellow text designates single numbers, and the red box is a 3×3 matrix with six independent parameters.

Attitude errors grow with time between star camera readings because of gyroscope rate noise and uncertainties in the transformation matrix (TM) between star cameras and gyroscopes. Although using the combination of star cameras and gyroscopes is common on pointed balloon-borne instruments, the employment of an extended 40 s scan between star camera images necessitated a detailed analysis of the system through simulations and the development of a judicious post-flight ADS to ensure that attitude errors met the requirement.

Star camera images provided attitude solutions that far exceeded the requirement. Between times for which images were available we integrated data from the gyroscopes; we refer to this as the integrated attitude (IA). Attitude errors for the IA originated from gyroscope slow-varying noise, which was a function of time, and from a time-independent inaccuracy in the TM between the gyroscopes and the star cameras’ frames of reference. There were two contributors to inaccuracy in the TM: an inaccuracy in the alignment matrix that orthogonalized

the gyroscopes—their hardware mounting was not perfectly orthogonal—and inaccuracy in the rotation matrix that rotated this orthogonalized frame to align with the star camera frame. Priors on the TM were obtained using preflight measurements of the gyroscope box orthogonality.

The ADS found both time-dependent and time-independent parameters through an algorithm that combined an Unscented Kalman Filter (UKF; Wan & van der Merwe 2000) and a least-squares optimizer, as shown in Figure 14. Using a given TM, the UKF determined the attitude and estimated the slowly time-varying gyroscope offsets. It ran forward and backward in time, producing a forward and a backward IA, as well as a solution that was the weighted average of the IA in each temporal direction. When each star camera measurement was made, the UKF computed the differences between the image solution and the forward and backward IA. The least-squares optimizer iteratively minimized these differences over the entire 11-day flight to find the optimal parameters of the time-independent

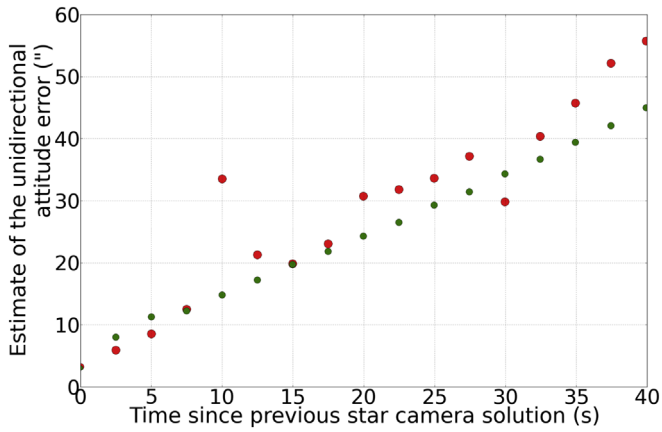


Figure 15. Estimate of the unidirectional attitude error $\sigma_{\Delta t}$ as a function of the time Δt since the last star camera solution. All throws are binned in 2.5 s bins. Data are shown up to $\Delta t = 40$ s because these encompass the majority of times. Values for the red circles are computed by collecting the differences between star camera solutions and unidirectional IA for all star camera images that fall within that bin. The value plotted is the standard deviation of the distribution in that bin. In green is plotted the unidirectional error estimated by the UKF, showing agreement with the measured data points.

TM. Each of the (multiprocessed) 90 iterations required to reach convergence took the equivalent of 80 minutes on a single 2.1 GHz processor. The error on the TM rotation and misalignment angles, evaluated by simulating sensors’ performance and reconstructing a known attitude and TM, were found to be within 3’4.

We evaluated the increase in attitude errors as a function of time separation Δt since the last star camera solution in the following way. For the forward or backward IA, which we call unidirectional IA, the error grew until a new star camera image was included in the solution, and the error at that sample was estimated using the difference between the unidirectional IA and the star camera solution, before the latter was included in the IA. We measured the error as a function of Δt by using pairs of star camera readings separated by that time. For each Δt , in bins 2.5 s wide, we histogrammed the differences between the star camera solution and that given by the IA. We included both forward and backward IA data points. The distribution means were near zero, but the standard deviations of the distributions $\sigma_{\Delta t}$ gave an estimate of the unidirectional attitude error at Δt away from a star camera solution. Figure 15 shows the unidirectional error $\sigma_{\Delta t}$ as a function of Δt for the EBEX2013 flight.

For the average attitude solution—constructed from the forward and backward IA—the attitude error $\sigma_{\Delta t}^A$ at any time since the last star camera solution was calculated using the unidirectional errors via

$$\frac{1}{(\sigma_{\Delta t}^A)^2} = \frac{1}{\sigma_{\Delta t}^2} + \frac{1}{\sigma_{(T-\Delta t)}^2}, \quad (1)$$

where T was the total time between star camera images. The error was largest midthrow and decreased close to the times the images were taken. Didier (2016) shows that, when the attitude errors of the average solution are translated into the ℓ domain using the EBEX2013 scan strategy, the spurious B -mode generated is less than 1/10 of the CMB lensing power spectrum for $\ell \leq 1500$.

4. Flight Management

The EBEX2013 flight marked the first use of a kilopixel array of TES bolometers aboard a balloon-borne payload. The short observation time available, the limited telemetry and commanding bandwidth, the modest available power and computing resources relative to a ground-based experiment, the large throughput of data, and the complexity of operating a kilopixel array required the development of (1) an efficient method to tune and control the TES bolometers; (2) specialized software to collect, store, and telemeter data; and (3) an onboard scheduling system to manage the multitudes of automated tasks that had to take place. Here we describe how we solved these challenges. More details are provided by MacDermid (2014) and Hillbrand (2014).

4.1. Onboard Computers

We used two redundant, ruggedized, low-power single-board computers.⁴⁴ Each computer had a 1.0 GHz Celeron processor, 256 MB RAM, and a 1 GB solid-state disk. The computers operated in ambient pressure and had a steady-state power consumption of 19.5 W each. The solid-state disk stored the computer operating system, additional modular drivers, and the FCP, which was configured to run immediately after the computer booted. The FCP, originally inherited from BLAST (Wiebe 2008) and heavily modified, controlled all aspects of payload operation, including scheduling observations, collecting data from the bolometer readout boards and from various housekeeping systems, storing data on board and telemetering to the ground, receiving commands from ground operators and distributing them to onboard subsystems, and occasionally triggering a set of commands that were preprogrammed before flight.

We developed an “event scheduler” that controlled all flight events. In its default mode, it controlled all onboard operations without operator interference. Various experiment events, such as planned sky observations and cycling of the sub-kelvin refrigerators, were preprogrammed and referenced to Coordinated Universal Time (UTC). The detailed sequence of commands necessary to conduct, for example, sky observations or a refrigerator cycle were stored in “schedule files” containing hundreds of individual commands. When triggering an event, the event scheduler launched and tracked the operation of the appropriate schedule file; when necessary, such as with sky observations, it operated with sidereal time. Ground operators also overrode the default scheduling, uploading alternate schedule files or triggering various predetermined schedule files.

Flight computer redundancy was implemented via a watchdog card⁴⁵ connected to the IEEE-1284 parallel port of each computer (Wiebe 2008). In nominal operation the FCP watchdog thread toggled a pin on the parallel port at 25 Hz. If this action ceased for more than 1 s, a fault was inferred and the watchdog card power-cycled the faulty computer and switched control to the other computer. The identity of the computer in control was communicated to both flight computers via a common bus and recorded. During the 11-day flight, we logged 19 noncommanded changes of the in-control computer, which we attribute to single-event upsets. Aside from these occasional reboots, both computers operated throughout the flight.

⁴⁴ AMPRO computers by ADLINK Technology, Inc.

⁴⁵ Provided by the University of Toronto.

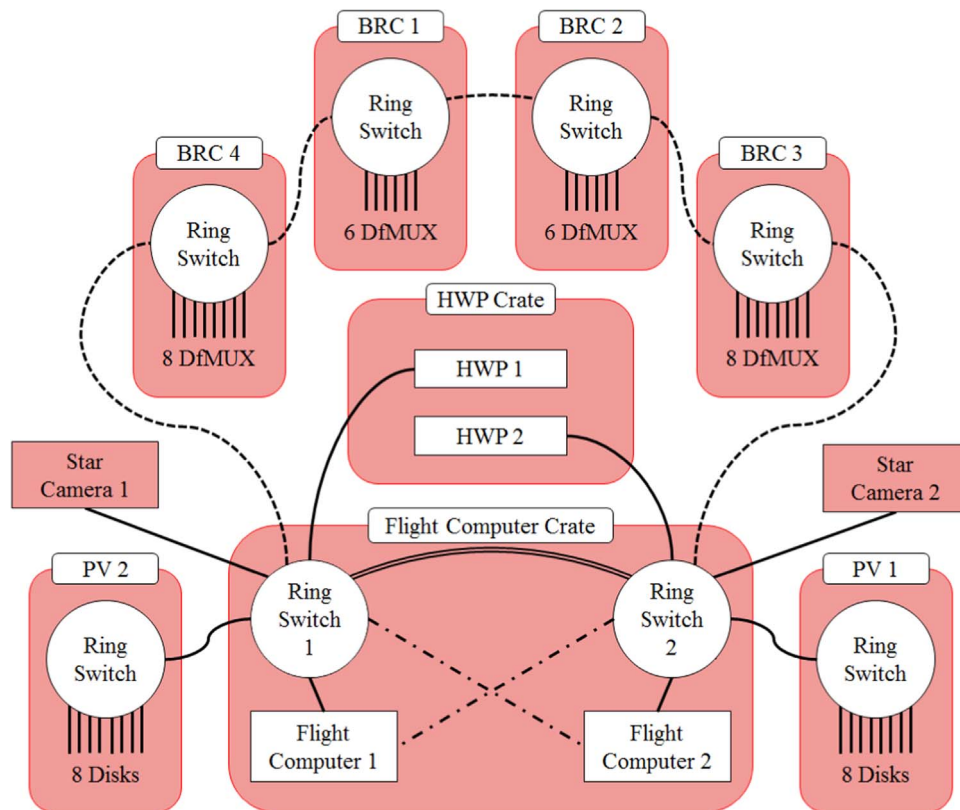


Figure 16. The EBEX ethernet network was based on a redundant ring structure consisting of eight ring switches. DfMUX boards in each of the BRCs communicated with a local ring switch. The four switches were connected with fiber-optic lines (dashed lines) to two ring switches in the flight computer crate, which communicated with their respective flight computers via copper line connection (solid lines). Standard copper lines also connected the flight computers with the HWP angle readout boards and the pressure vessel (PV) that were used to store data. If any of the BRC ring switches or fiber-optic lines malfunctioned, data from the other BRCs would still reach the flight computers. If one of the flight computer switches malfunctioned, a fail-over line activated (double line) that would pass data from the fiber-optic line to the other switch, and another fail-over line activated (dot-dashed lines), connecting the nonfaulty switch to both flight computers.

4.2. Timing System

Data collected by the various flight subsystems, including flight computers, the ACS, the receiver housekeeping system, and the detector readout system, were stamped by each subsystem asynchronously. We synchronized these subsystems using a common time system, called EBEXTime, described below. Additional details are provided in Sagiv (2011).

The time synchronization system consisted of a time server and various time clients. Communication with the time server was handled via a Controller Area Network bus (CAN bus) card. There were two time servers on board for redundancy; thus, there were EBEXTime1 and EBEXTime2. The boards were connected to the BRCs and the ACS electronics clients via an RS-485 serial line and to the receiver housekeeping electronics and the flight computer clients via a CAN bus.

EBEXTime is the number of $10 \mu\text{s}$ ticks since the start of a “major period,” which was at most 6 hr in duration. The major period counter was stored in nonvolatile EEPROM on the timing server board. A new major period started each time the time server was powered on. The flight computer could optionally set the time server’s major period upon power-up initialization. The full EBEXTime datum was a 48-bit word consisting of a 2-bit Board ID, a 14-bit major period register, and a 32-bit tick counter. Each time client maintained its own copy of the EBEXTime. Each client’s 32-bit tick counter was incremented by a local oscillator at 100 kHz. The time server, at a rate of 6.1 Hz ($0.16384 \text{ s} = 214 \text{ ticks}$), broadcasted a synchronization message consisting of its board ID and the

high 32 bits (i.e., the major period and the high 18 bits of the tick counter) to all clients. On receipt of a valid synchronization message the client rewrote its 46-bit time word with the 32 bits received plus 14 zero bits appended. Local client clocks used oscillators with ± 25 ppm stability. The master clock on the time server used an oven-controlled oscillator with a temperature stability of ± 0.2 ppb between -20°C and $+70^\circ\text{C}$.

Upon power-up, clients used either of the time servers’ synchronization messages available on their bus. They automatically switched to the other if one became unavailable. Both time servers were synchronized to absolute time post-flight using the in-control flight computer CPU time. Because the entire attitude solution was conducted in equatorial coordinates and all data were co-stamped with EBEXTime together with the attitude solutions, only very coarse (tens of minutes) synchronization with absolute time was necessary.

4.3. Onboard Network

We used a TCP/IP network to pass bolometer, HWP, and star camera data to the flight computers. All data, including those passed to the flight computers using dedicated non-TCP/IP buses, were channeled using TCP/IP to two pressure vessels that held data storage disks; see Figure 16. The network employed a redundant ring switch technology.⁴⁶ Each of the 28 DfMUX readout boards was connected via category 5e ethernet cables to a single ring switch inside its respective BRC. The

⁴⁶ Sixnet Series from Red Lion, Inc.

individual ring switches were linked together via fiber-optic lines in a redundant ring that encompassed the four readout crates and two ring switches in the flight computer crate. Severing a communication link to any of the four readout crates caused the ring switch network to engage its backup link between the two ring switches in the flight computer crate. Systems that were connected to the overall network by nonredundant links were themselves redundant with other systems. As such, flight critical disruptions to the data network required at least two concurrent, critical errors.

4.4. Telemetry

Telemetry was provided over three distinct pathways: line-of-sight communications, tracking and data relay satellites (TDRSS), and the Iridium satellite phone network. Line-of-sight communication was available only for the first ~ 24 hr of the flight and had a bandwidth of 1 Mbit s^{-1} . Communication via the TDRSS satellites was scheduled approximately 24 hr in advance for several hours per day. When operational, it had variable bandwidth between 6 and 75 kbits s^{-1} and was used for both uplinking commands and downlinking data. The Iridium phone network was available continuously with a bandwidth of 2 kbits s^{-1} . It was used only for commanding. Because the downlink bandwidth was variable, ground operators commanded the flight computer to throttle telemetry down to match the available bandwidth. The onboard throttling software relied on two elements: data compression and priority-based data downlinking.

We used a statistical data compression scheme, based on the Z-Coder (Bottou et al. 1998) adaptive binary coder. This compression was based on a statistical model of the bit structure of the data. While standard statistical compression forms the model based only on the data available at the time of compression, the EBEX compressor was pretuned to the expected form of the data streams. These data streams included bolometer and HWP data, which were stored as 16-bit, big-endian time streams; JavaScript Object Notation formatted strings generated by array tuning commands; text-based miscellaneous log file data; and 16-bit, little-endian house-keeping and attitude control data. Each characteristic data stream was analyzed preflight, and statistical models were generated and stored on the flight computer for use during flight. The flight control software was responsible for selecting the appropriate compression model based on the source of the data stream. Because the compression was still adaptive, the consequence of the flight data being different from the ground “training set” was merely to decrease the effective compression ratio. The compression ratio for the ground “training set” data was 10.1. Flight data showed a compression ratio of 6.2 for the bolometer data and between 7 and 10 for other data products.

The compressed data were segmented into bundles of prioritized types. The flight software ordered these bundles by priority and fed them into the downlink stream. Ground operators occasionally changed the priority structure using standard commands so as to allow for different priorities during different phases of the flight. For example, HWP data were prioritized when turning the rotation on/off, pointing information when maneuvering the attitude of the telescope, and bolometer time stream data during regular observations.

4.5. Tuning and Controlling the Detector Array

Operating the TES bolometer array required tuning the bias currents in each of the 128 SQUID preamplifiers for optimal trans-impedance (MacDermid et al. 2009). It also required tuning the electrical bias of each of the ~ 1000 detectors such that they were operated at the superconducting transition temperature. In practice, tuning required sending a sequential set of instructions to hardware components that resulted in raising and lowering the temperature of the SQUIDs, adjusting the current flowing through them, and adjusting the voltage bias of the bolometers. A specific set of tuning instructions is referred to as a “tuning algorithm.” Each of the 28 DfMUX electronic boards that control and read out the detectors and SQUIDs had the task of interpreting the instructions, generating the appropriate voltages and currents, and collecting data. (Section 4 of EP2 provides additional details about the readout system and the DfMUX boards.)

In a typical ground-based experiment, a central control computer cycles through each step in the algorithms for each of the SQUIDs and TESs, sends commands to modify the configuration of the readout boards, and collects and stores the data. Because of the limited uplink bandwidth, we developed an efficient way to address each of the SQUIDs and detectors in the array. Because of the limited computing power available, we transferred execution of the tuning algorithms from the flight computers to each of the 28 electronic boards controlling the SQUIDs and TES detectors. Finally, limited downlink bandwidth required that we economize diagnostic data sent to the ground as a result of tuning the array. We now describe each of these developments.

4.5.1. Addressing SQUID and TES Commands

To efficiently address an individual TES or SQUID, we constructed a “hardware map” that stored the mapping between each TES, its readout SQUID, its DfMUX board, and all other readout components. It also stored the preselected parameters to set up the entire array, determined during preflight testing.

The hardware map was stored as a series of linked tables in an sqlite3 database (Newman 2004) on the internal disk on each of the two flight computers. Tuning commands were then targeted to any arbitrary subsection of the hardware by forming a request using structured query language (SQL) commands. Such commands were generated automatically on board the flight computer during prescheduled tunings of the array or, as necessary, by ground operators.

The SQL commands had the advantage that they were sufficiently compact to fit in the 250-byte maximum command length set by the CSBF uplink protocol and still flexible enough to provide ground operators full manual tuning capability. For example, after the first tuning at float we discovered that a significant fraction of detector biases, over 70%, needed to be adjusted. This was anticipated preflight, as we lacked a sufficiently accurate estimate of the millimeter-wave emission of the atmosphere. The SQL commands enabled flexible and relatively rapid retuning of the array and storage of new default parameters for each detector.

4.5.2. Executing the Tuning Algorithms

We transferred the responsibility of executing the tuning algorithms from a central computer to the DfMUX boards. A library of tuning algorithms written in Python was loaded onto

a flash memory card installed on each of the DfMUX boards. The commands arriving from the onboard computer consisted of a single instruction for an entire tuning algorithm, instead of a line-by-line cycle through the algorithm itself. When such a command arrived, the resident MicroBlaze soft processor running on the DfMUX board's FPGA⁴⁷ executed the algorithm (MacDermid 2009). An “algorithm-manager” program running on the MicroBlaze delegated the tuning to several processes that ran as parallel threads. This allowed multiple TES bolometers connected to the same DfMUX board to be tuned simultaneously, saving tuning time. Tuning algorithms that were executed on different boards were always executed in parallel. Therefore, total array tuning time was independent of the size of the array.

4.5.3. Handling Diagnostic Data

Each tuning algorithm collected diagnostic data on the components it tuned, such as the $I - V$ characteristics of each bolometer as it was biased into its superconducting transition. The entirety of the tuning data were stored on board, as they were vital for understanding the performance of the bolometer array during post-flight analysis. The data were also important for monitoring and tuning the bolometer array during flight, but sufficient telemetry bandwidth was not always assured. We therefore used the telemetry prioritization scheme described in Section 4.4. After each tuning algorithm completed execution, we first downlinked the current state of the DfMUX boards' settings. Ground operators compared the current end-of-algorithm state of the boards to the initial pre-algorithm execution state to ascertain that the algorithm was in fact executed. We then prioritized downlinking the entire data available for each of the tuning algorithms. These data had the highest priority while any array tuning activities took place, as there were no other scientifically interesting data available during that time. To quickly digest and act upon the influx of tuning data, we wrote custom software that automatically analyzed them and made the results available in automatically generated web pages (MacDermid 2014). Ground operators used the results to plan the subsequent actions required to optimize the performance of the bolometer array.

In many cases some of the tuning data were not fully downlinked by the time we resumed science observations, at which time attitude control and detector time stream data received higher telemetry priority. Array tuning data that received lower downlink priority typically trickled down over several hours after the completion of the tuning operation.

4.6. Data Management

We designed the data management and storage system to handle all the data that could be collected by the 1792 readout channels available with the 28 DfMUX electronic readout boards. With 16 bits per sample and a sampling rate of 190.735 Hz, the anticipated data rate was 5.5 Mbits s^{-1} accumulating to 590 GB over 10 days of flight. At the time we designed the system, this volume exceeded the capacity of any single, commercially available hard drive. We therefore designed two redundant disk arrays based on Advanced Technology Attachment (ATA) over Ethernet (AoE) protocol. Each array contained a full copy of all flight data, including

science data, system logs, attitude sensor data, and house-keeping information. All data were written to disk in a standardized packet format. All packets had a header with information that included data source identification—for example, bolometer identifier or temperature sensor identifier—and a time stamp.

Each array had seven 320 GB commercial 2.5 parallel ATA magnetic hard disks. Three disks were sufficient to hold a complete copy of the preflight and flight data, with ample margin; the other disks were designed to remain empty and be used only in case of disk hardware failure. Each array was housed in a separate pressure vessel in which we maintained atmospheric pressure and circulated the air with two fans. (We decided to not use solid-state memory owing to cost and concerns about the robustness of this hardware under the elevated cosmic-ray flux at float altitude.) During preflight integration and testing, vibrations from the fans initially induced repeated disk failures. Decoupling the fan mounting from the structure holding the disks eliminated disk failures. Following this modification, we did not experience any further disk failure throughout integration of the instrument or flight. The hard drives were mounted on printed circuit boards called Blade II that implemented the AoE protocol.⁴⁸ We found that, with the Blade II, the rate at which data were written to disk declined approximately linearly with an increase in the number of files being written simultaneously. We combined similar data streams into the same files, resulting in a maximum of 31 files open at any given time. At this level the writing rate was adequate and no data were lost as a result of pileups.

We developed custom disk management software that wrote data to a single disk within the array to minimize power consumption by keeping all other disks idle. Steady-state power consumption was measured to be 38.4 W per disk pressure vessel. The software maintained information about the current state of each disk, including its error count, free space, and response speed. Using these data, the software selected the best available disk on startup and wrote all data to the same disk until it either filled or failed. The software then selected the next available disk, mounted the new disk in a background process, and moved data streaming to the new disk. During the transition, which was measured to take 5 s, data were buffered; buffer depth allowed for 75 s of data storage.

5. Summary

To probe the CMB E - and B -modes with higher sensitivity compared to previous instruments and at frequency bands not accessible for ground observatories, we built EBEX, a stratospheric balloon-borne instrument with approximately 1000 detectors and designed for long-duration Antarctic flights.

EBEX pioneered the use of TES bolometers on a balloon-borne platform. It was the first experiment to fly a small array of these detectors in a test flight in 2009 and a kilopixel array during its EBEX2013 flight. Nearly 1000 TES bolometers were operating shortly after the payload reached float altitude, and subsequent refrigerator cycles and array tuning operations could proceed with little ground-operator intervention.

The platform presented unique challenges in computing power, bandwidth, and duration of observation time. To meet these challenges, we developed a flexible flight event scheduler, an onboard network, a tuning and control software

⁴⁷ Virtex-4 FPGA by Xilinx Inc.

⁴⁸ Coraid, Inc.

based on SQL commands, a prioritized telemetry downlink, and an efficient method to implement all array tuning commands.

To limit the number of wires reaching the lowest-temperature cryogenic stage, we decided to multiplex the readout of several detectors onto a single pair of bias and readout wires. We chose frequency domain multiplexing (Dobbs et al. 2012)—as opposed to time domain multiplexing (Henderson et al. 2016)—because it required fewer wires at the lowest-temperature stage, simplifying the design of the cryogenic receiver. This decision moved the design and implementation challenge from optimizing the cryogenic stage to two other aspects: (1) developing a frequency domain multiplexing system that had lower power consumption compared to the system available at the time the project began, and (2) providing and dissipating the still-appreciable level of heat generated by the new system. We pioneered the implementation of the DfMUX system, now used by a number of other experiments; this is discussed more fully in EP2. We described the EBEX power system that could provide more than 2.3 kW for a calculated peak load of 1.7 kW, of which 590 W was consumed by the readout system. Much of the power dissipation was localized in a few electronic components. Conduction, heat pipes, and a liquid cooling loop were used to transfer the energy to panels that radiated it to the sky. In-flight performance matched preflight predictions and showed that all electronic boards stayed within their nominal operating temperatures.

The optical system, including both telescope and receiver, which was sized to accommodate the kilopixel array and to reach 6' resolution, led to an 8 m tall gondola and a payload weight of 2810 kg that, together with NASA equipment, approached the balloon load limit of 3600 kg. We gave an overview of the mechanical structure of the EBEX gondola. A number of measures to reduce weight are described throughout the series of three papers. One of them was the use of polyethylene suspension cables as part of the gondola structure. To our knowledge, this is the first use of such cables in a stratospheric, long-duration balloon payload. The EBEX2013 experience indicates that these cables are suitable for balloon flights as long as proper consideration is given to their UV sensitivity and initial creep.

Telescope elevation motion was achieved by moving the inner relative to the outer frame with a linear actuator. We described a mechanism to lock the inner relative to the outer frame and thus reduce risk of damage to the linear actuator from launch accelerations. We controlled azimuth motion with a pivot and a reaction wheel. A thermal model error caused the pivot motor controller to overheat and turn off when attempting to execute the design scan strategy. Free gondola azimuth motion consisted of a superposition of full rotations at variable rotational speed and an 80 s period oscillatory motion at the natural torsional period of the flight line and gondola. We therefore chose to fix the elevation, giving a sky scan consisting of a 5700 deg² strip in DEC.








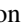
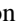





We described the EBEX2013 attitude determination system, which relied on star cameras, gyroscopes, a custom-built star camera software STARS, and an attitude reconstruction software. The in-flight sky scan, with nearly zero azimuth speed occurring approximately every 40 s, matched the preflight plans for attitude reconstruction. The reconstruction software was used to minimize attitude errors and to assess their contribution to spurious *B*-modes. The combination of

hardware, STARS, and the attitude reconstruction software constrained attitude errors such that the spurious *B*-modes they induced are less than 10% of predicted CMB *B*-modes with $r = 0.05$ for $30 \lesssim \ell \lesssim 1500$.

Two companion papers provide additional details about the EBEX instrument's telescope, receiver, and polarimetry (EP1) and the detectors, their readout, and their flight performance (EP2).

Support for the development and flight of the EBEX instrument was provided by NASA grants NNX12AD50G, NNX13AE49G, NNX08AG40G, and NNG05GE62G and by NSF grants AST-0705134 and ANT-0944513. P.A., L.M., E.P., and C.T. acknowledge the Science & Technology Facilities Council for its continued support of the underpinning technology for filter and wave plate development. We also acknowledge support by the Canada Space Agency, the Canada Research Chairs Program, the Natural Sciences and Engineering Research Council of Canada, the Canadian Institute for Advanced Research, the Minnesota Supercomputing Institute at the University of Minnesota, the National Energy Research Scientific Computing Center, the Minnesota and Rhode Island Space Grant Consortia, our collaborating institutions, and Sigma Xi, The Scientific Research Society. C.B. acknowledges support by the RADIOFOREGROUNDS project, funded by the European Commissions H2020 Research Infrastructures under grant agreement no. 687312, as well as the Italian INFN INDARK initiative. J.D. acknowledges a NASA NESSF fellowship NNX11AL15H. K.H. acknowledges NASA NSTRF fellowship NNX11AN35H. B.R.-K. acknowledges an NSF Post-Doctoral Fellowship AST-1102774 and a NASA Graduate Student Research Fellowship. K.R. and K.Z. acknowledge support by the Minnesota Space Grant Consortium. We very much thank Danny Ball and his colleagues at the Columbia Scientific Balloon Facility for their dedicated support of the EBEX program. We thankfully acknowledge contributions to predicting systematic errors by Matias Zaldarriaga and Amit Yadav. We thank the BLAST team for providing the original version of the flight computer program discussed in Section 4. We thank Christopher Geach, Qi Wen, and Xin Zhi Tan for help with figures.

ORCID iDs

Peter Ade  <https://orcid.org/0000-0002-5127-0401>
 Derek Araujo  <https://orcid.org/0000-0003-0527-2948>
 François Aubin  <https://orcid.org/0000-0002-8241-4156>
 Joy Didier  <https://orcid.org/0000-0003-4151-9450>
 Shaul Hanany  <https://orcid.org/0000-0002-8702-6291>
 Kyle Helson  <https://orcid.org/0000-0001-9238-4918>
 Andrew Jaffe  <https://orcid.org/0000-0003-2086-1759>
 Lorne Levinson  <https://orcid.org/0000-0003-4679-0485>
 Michele Limon  <https://orcid.org/0000-0002-5900-2698>
 Lorenzo Moncelsi  <https://orcid.org/0000-0002-4242-3015>
 Ilan Sagiv  <https://orcid.org/0000-0001-8377-3153>
 Gregory S. Tucker  <https://orcid.org/0000-0002-6954-6947>
 Karl Young  <https://orcid.org/0000-0002-1337-6088>
 Kyle Zilic  <https://orcid.org/0000-0003-1971-7151>

References

- Ade, P., Akiba, Y., Anthony, A., et al. 2014, *ApJ*, 794, 171
 Aubin, F. 2012, PhD thesis, McGill Univ.
 Aubin, F., Aboobaker, A. M., Ade, P., et al. 2010, *Proc. SPIE*, 7741, 1T
 Aubin, F., Aboobaker, A. M., Ade, P., et al. 2016, arXiv:1601.07923

- Baumann, D., Jackson, M. G., Adshead, P., et al. 2009, in AIP Conf. Ser. 1141, CMB Polarization Workshop: Theory and Foregrounds (Melville, NY: AIP), 10
- BICEP2 Collaboration, Ade, P. A. R., Aikin, R. W., et al. 2014, *PhRvL*, 112, 241101
- BICEP2/Keck and Planck Collaborations, Ade, P. A. R., Aghanim, N., et al. 2015, *PhRvL*, 114, 101301
- Bottou, L., Howard, P. G., & Bengio, Y. 1998, in IEEE Data Compression Conference, 672124
- Chapman, D. 2015, PhD thesis, Columbia Univ.
- Chapman, D., Aboobaker, A., Araujo, D., et al. 2015, in IEEE Aerospace Conf., 7119013
- Chapman, D., Didier, J., Hanany, S., et al. 2014, *Proc. SPIE*, 9152, 12
- Didier, J. 2016, PhD thesis, Columbia Univ.
- Didier, J., Chapman, D., Aboobaker, A., et al. 2015, in IEEE Aerospace Conf., 7119010
- Dobbs, M. A., Lueker, M., Aird, K. A., et al. 2012, *RSci*, 83, 073113
- Grainger, W., Aboobaker, A. M., Ade, P., et al. 2008, *Proc. SPIE*, 7020, 2N
- Hanson, D., Hoover, S., Crites, A., et al. 2013, *PhRvL*, 111, 141301
- Henderson, S. W., Stevens, J. R., Amiri, M., et al. 2016, *Proc. SPIE*, 9914, 1
- Hillbrand, S. 2014, PhD thesis, Columbia Univ.
- Hu, W., Hedman, M. M., & Zaldarriaga, M. 2003, *PhRvD*, 67, 043004
- Klein, J., Aboobaker, A., Ade, P., et al. 2011, *Proc. SPIE*, 8150, 04
- Kovac, J. M., Leitch, E. M., Pryke, C., et al. 2002, *Natur*, 420, 772
- MacDermid, K. 2009, Master's thesis, McGill Univ.
- MacDermid, K. 2014, PhD thesis, McGill Univ.
- MacDermid, K., Aboobaker, A. M., Ade, P., et al. 2014, *Proc. SPIE*, 9153, 11
- MacDermid, K., Hyland, P., Aubin, F., et al. 2009, *AIPC*, 1185, 253
- Milligan, M., Ade, P., Aubin, F., et al. 2010, *Proc. SPIE*, 7740, 07
- Naess, S., Hasselfield, M., McMahon, J., et al. 2014, *JCAP*, 2014, 007
- Newman, C. 2004, SQLite (Developer's Library) (Indianapolis: Sams)
- Oxley, P., Ade, P. A., Baccigalupi, C., et al. 2004, *Proc. SPIE*, 5543, 320
- Pascale, E., Ade, P., Bock, J., et al. 2008, *ApJ*, 681, 400
- Polsgrove, D. E. 2009, PhD thesis, Univ. Minnesota
- Rabii, B., Winant, C. D., Collins, J. S., et al. 2006, *RSci*, 77, 071101
- Reichborn-Kjennerud, B. 2010, PhD thesis, Columbia Univ.
- Reichborn-Kjennerud, B., Aboobaker, A. M., Ade, P., et al. 2010, *Proc. SPIE*, 7741, 1C
- Sagiv, I., Aboobaker, A. M., Bao, C., et al. 2012, in 12 Marcel Grossmann Meeting, ed. A. H. Chamseddine (Singapore: World Scientific Publishing), 2166
- Sagiv, I. S. 2011, PhD thesis, Univ. Minnesota
- Scott, D., & Smoot, G. F. 2010, arXiv:1005.0555
- Soler, J. D., Ade, P. A. R., Angilè, F. E., et al. 2014, *Proc. SPIE*, 9145, 34
- The EBEX Collaboration, Abitbol, M., Aboobaker, A. M., et al. 2018b, *ApJS*, 239, 8
- The EBEX Collaboration, Aboobaker, A. M., Ade, P., et al. 2018a, *ApJS*, 239, 7
- Wan, E. A., & van der Merwe, R. 2000, in IEEE Adaptive Systems for Signal Processing, Communications, and Control Symp., 882463
- Westbrook, B., Lee, A., Meng, X., et al. 2012, *JLTP*, 167, 885
- Westbrook, B. G. 2014, PhD thesis, Univ. California, Berkeley
- Wiebe, D. V. 2008, PhD thesis, Univ. Toronto
- Zaldarriaga, M., & Seljak, U. 1997, *PhRvD*, 55, 1830
- Zilic, K. 2014, PhD thesis, Univ. Minnesota